Variscan high-pressure metamorphism of kyanite-bearing paragneisses hosting eclogites in the Veporic unit, Western Carpathians: Evidence from Th–U–Pb dating of monazite

IGOR PETRÍK[1,✉], MARIAN JANÁK[1], TOMÁŠ VACULOVIČ[2], PATRIK KONEČNÝ[3] and ŠTEFAN MÉRES[4]

[1]Earth Science Institute, Slovak Academy of Sciences, Dúbravská cesta 9, 840 05 Bratislava, Slovakia;
✉igor.petrik@savba.sk, marian.janak@savba.sk
[2]CEITEC, Masaryk University, Brno, Czech Republic
[3]Dionýz Štúr State Geological Institute, Mlynská dolina 1, 817 04 Bratislava, Slovakia
[4]Department of Geochemistry, Faculty of Natural Sciences, Comenius University, Ilkovičova 6, 84215 Bratislava, Slovakia

Abstract: In view of a polyphase development of the northern Veporic pre-Alpine basement of the Western Carpathians it is important to determine the age of high pressure (HP) metamorphism known from eclogites occurring in this area. To do this, several monazite-bearing paragneisses were studied petrologically and monazite was dated by chemical (U–Th–Pb) method. Identified were remnants from high-pressure stage, i.e. phengite (Si apfu=3.2–3.3), kyanite, rutile and Ca-rich garnet rims. Part of the present mineral assemblage may have been preserved from prograde stage (plagioclase) and part reflects re-equilibration during retrogression (biotite, major elements in garnet cores). However, Y and HREE in garnet cores were not homogenised and their profiles indicate origin during temperature rise. Peak metamorphic conditions (P=21 kbar; T=650 °C), and retrogression stage (P=9 kbar; T=520 °C) were calculated using Zr-in-rutile, and Y-in-garnet and monazite thermometry, phengite composition and pseudosection modelling. Monazite yielded dominant Early Carboniferous age (354 Ma) with subordinate amounts of Ordovician (485 Ma) and Cambrian (505 Ma) ones, and no Alpine record. The monazite position in garnet cores predating the growth of Ca rims suggest that the Carboniferous age of 354 Ma probably predates the peak conditions and refers to the prograde stage of the Variscan metamorphic evolution.

Keywords: monazite, Th–U–Pb dating, high-pressure metamorphism, Variscan orogeny, Veporic unit, Western Carpathians.

Introduction

The pre-Alpine basement of the Western Carpathians is an important segment of the Variscan orogeny in Europe, which marks the collision of Laurasia with Gondwana-affiliated terranes during the Paleozoic. Evidence for subduction and high-pressure (HP) metamorphism comes from eclogites, which are mostly retrogressed to garnet amphibolites and occur in all major tectonic units – Tatric, Veporic and Gemeric (Hovorka & Méres 1990; Hovorka et al. 1992; Janák et al. 1996, 2007, 2009; Janák & Lupták 1997; Faryad et al. 2005, 2020), and rarely metaultramafites in the Veporic unit (Janák et al. 2020). Peak *P–T* conditions of eclogites and metaultramafites in the pre-Alpine basement of the Veporic unit attained 2.5 GPa and 700 °C (Janák et al. 2007, 2020) suggesting subduction to depths of about 80 km during the Variscan orogeny. The Sm/Nd dating of garnet from retrogressed eclogite in the Western Tatra (Tatric Unit) yields Variscan (Early Carboniferous) age of 342 Ma (Moussallam et al. 2012), however, such geochronological data on Veporic eclogites or metaultramafic rocks are lacking. Metasedimentary gneisses hosting eclogites and metaultramafites may provide evidence on age of metamorphism through dating of accessory minerals such as zircon or monazite and thus constrain the *P–T–t* history.

Monazite is one of the most informative minerals in felsic crustal rocks, providing information not only on the age of metamorphic events but also through its chemistry (LREE, Th, U, Y) on equilibria with metamorphic phases such as garnet and feldspars (e.g. Finger et al. 1998; Zhu & O'Nions 1999; Terry et al. 2000; Catlos et al. 2002; Spear & Pyle 2002; Hermann & Rubatto 2003; Kohn et al. 2005; Krenn et al. 2009; Gieré et al. 2011; Majka et al. 2012; Petrík et al. 2016, 2019; Engi 2017; Hacker et al. 2019). Previous electron microprobe dating of monazite in gneisses from the North Veporic basement (Janák et al. 2002; Petrík et al. 2017) yielded two groups of ages. The older one (ca. 470 Ma) was interpreted as recording pre-Variscan (Ordovician) magmatism, whereas the younger one (ca. 340 Ma), as Variscan (Carboniferous) metamorphism.

In this article, we present results of new, more extensive Th–U–Pb dating of monazite in kyanite–garnet paragneisses from the North Veporic basement along with petrological interpretation based on thermodynamic modelling. Monazite was analysed by electron microprobe in situ, allowing domains

of <5µm size to be measured and dated by MARC (monazite age reference correction) method developed in the Dionýz Štúr State Geological Institute in Bratislava (Konečný et al. 2018), for details see analytical techniques.

Geological background

The investigated paragneisses occur in the northern part of the Veporic unit (Fig. 1), where the pre-Alpine basement is overlain by an Upper Paleozoic–Triassic sedimentary cover. The magmatic and metamorphic history of the Veporic unit was polyphase, comprising pre-Variscan, Variscan, Permian and Alpine events (e.g. Bezák et al. 1997; Plašienka et al. 1997; Putiš et al. 1997; Janák et al. 2001; Jeřábek et al. 2008a; Vojtko et al. 2016; Plašienka 2018).

The northern part of the Veporic unit is composed of several basement complexes covered by Permian and Mesozoic rocks (Fig. 1). The eclogites are part of the basement that is variously referred to as the Hron complex (Klinec 1966), leptyno–amphibolite complex (Hovorka et al. 1994, 1997) or layered metaigneous complex (Putiš et al. 1997). In this paper we use the term "leptyno–amphibolite complex" (LAC). In the investigated area, the LAC is composed of several rock types, the most abundant of which are amphibolites and gneisses (both ortho- and para-gneisses) that are strongly deformed and retrogressed to epidote amphibolites, mica schists and phyllites. Garnet amphibolites with relics of eclogites and ultramafic rocks (olivine gabbro, troctolite) occur in sporadic outcrops of metre to tens of metres size (Ivan et al. 1996; Méres et al. 1996; Janák et al. 2007). Pre-Alpine granitoids and associated gneisses to the east of the studied area (Fig. 1)
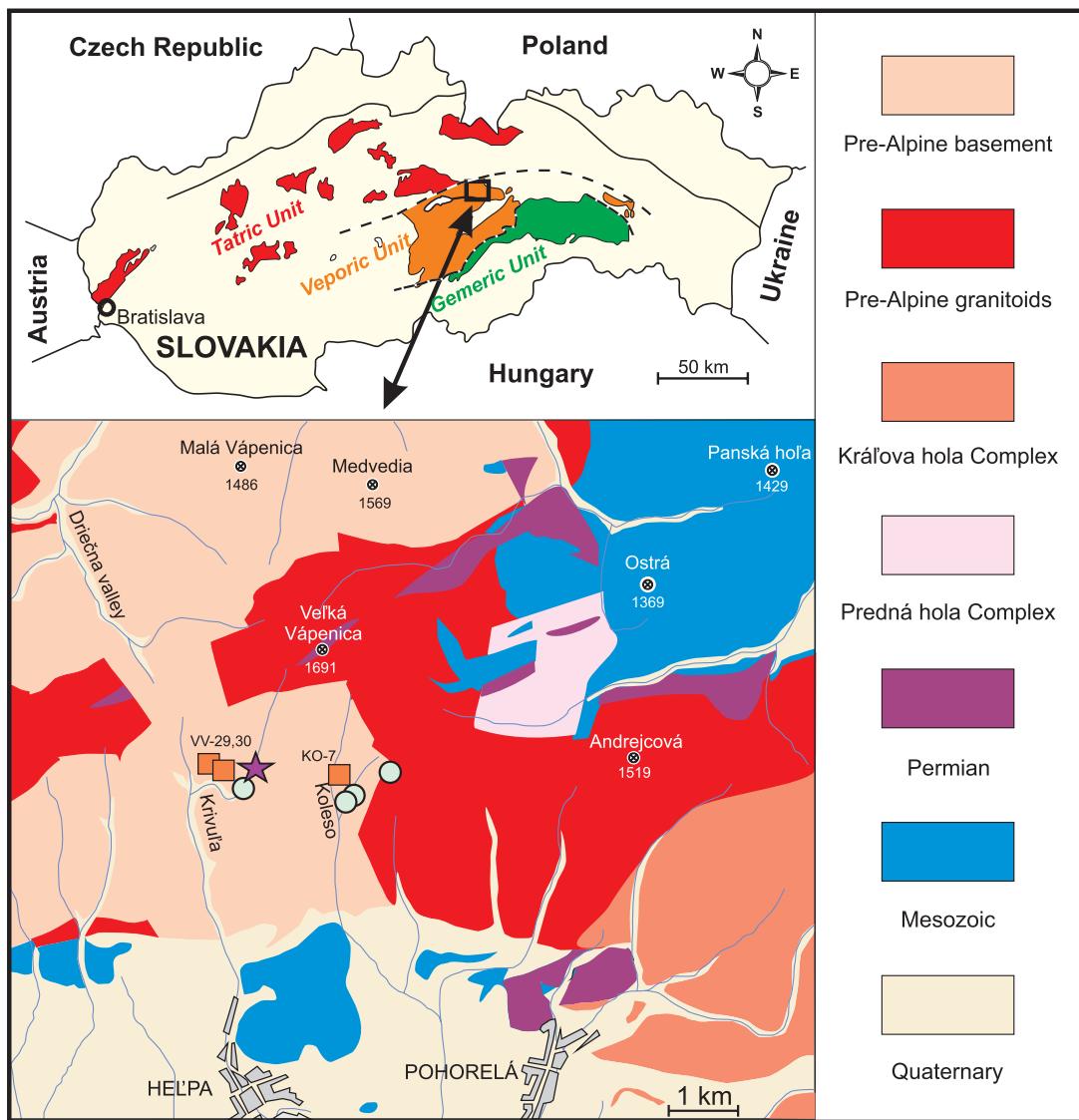

Fig. 1. Simplified geological map of the northern parts of the Veporic unit (modified from Biely et al. 1992) showing the locations of the investigated kyanite-bearing paragneisses (box). Eclogites (Janák et al. 2007) are marked by circle and HP metaultramafite (Janák et al. 2020) by star.

and mica schists belonging to the Kráľova hoľa complex were strongly affected by Alpine mylonitization. The intrusion age of these granitoids is 350 Ma, based on SHRIMP dating of zircons (Gaab et al. 2006). Zircon dating of the orthogneisses revealed various pre-Variscan (Cadomian, Cambrian, Ordovician) magmatic and metamorphic ages and Variscan (Carboniferous) metamorphic overprint (Gaab et al. 2006; Putiš et al. 2008). The Variscan age (350 Ma) of northern Veporic granitoids was recently confirmed by titanite dating of Sihla tonalite (Uher et al. 2019). ^{40}Ar–^{39}Ar dating of amphiboles from the northern Veporic unit yielded mostly pre-Alpine ages (Kráľ et al. 1996).

The Predná hoľa complex is composed of phyllites, metasandstones, basic volcanics and volcanoclastics that were recrystallized at low grades of metamorphism. Permian rocks include metamorphosed conglomerates, sandstones, arkoses and greywackes locally with volcanogenic material. Mesozoic rocks consist of Triassic carbonates and quartzites that were affected by Alpine low-grade metamorphism in Cretaceous time (Lupták et al. 2003). In contrast, Alpine metamorphism in the southern part of the Veporic unit resulting from crustal thickening in Cretaceous time attained maximum P–T conditions of 1–1.2 GPa and 600–620 °C (Janák et al. 2001; Jeřábek et al. 2008b, 2012).

Analytical techniques

Electron microprobe WDS analysis of mineral chemistry was performed with a CAMECA SX-100 electron microprobe housed in the Dionýz Štúr State Geological Institute in Bratislava. The analytical conditions were as follows: 15 kV accelerating voltage and 20 nA beam current, peak counting time 20 s, and beam diameter of 2–10 μm. Raw counts were corrected using the on-line PAP routine. Mineral standards (Si, Ca: wollastonite, Na: albite, K: orthoclase, Fe: fayalite, Mn: rhodonite), pure element oxides (TiO_2, Al_2O_3, Cr_2O_3, MgO), and metals (Ni) were used for calibration.

Zirconium concentrations in rutile were measured by electron microprobe JEOL JXA 8530F in the Earth Science Institute, Slovak Academy of Sciences in Banská Bystrica. Chemical composition of rutile was determined using wavelength-dispersive spectrometry (WDS) at following conditions: accelerating voltage 15 kV, probe current 150 nA. Beam diameter varied from 3 to 7 μm depending on the grain size of rutile. Calculation of concentration was provided by ZAF correction method. For measurements of trace elements in rutile the minerals and synthetic compounds were used as standards. The H- and L-types of spectrometers were chosen for measuring Zr due to their highest sensitivity for this element.

Monazite was dated by the MARC (monazite age reference correction) method developed in the Dionýz Štúr State Geological Institute in Bratislava (Konečný et al. 2018), using microprobe analyses from CAMECA SX 100. Spot monazite analyses were acquired with conditions of 15 kV accelerating voltage, 180 nA beam current, and 3 μm beam diameter with the aim of increasing counting both efficiency and spatial resolution. Long counting times were used to increase analytical precision: for Pb – 300 s peak and 2×150 s backgrounds, Th – 35 s peak and 2×17.5 s background, U – 80 s peak and 80 s background, Y – 40 s peak and 2×20 s background. Calibration reference materials of REE's and Y were phosphates synthesized by Daniel Harlov at the GFZ German Research Centre, Potsdam, Germany: Pb – $PbCO_3$, Th – ThO_2, U – UO_2, S – barite, Ca – wollastonite, Sr – $SrTiO_3$, Al – Al_2O_3, Si – wollastonite and Fe – fayalite. Sequential measurement on the spectrometer in the order Pb, Th, U, Y (large PET) was corrected for acquisition time of these elements. Naturally curved background at Pb-Mα was estimated by a novel method (Konečný et al. 2018). Mutual interferences were resolved by an empirical correction, which included matrix effects on both reference material and on unknown sample. Age estimates were tested on monazites dated by methods of isotopic ratios of Pb and U, called age reference materials (ARM). A set of 10 ARM's was utilized for assessment of minor systematic errors that cannot be suppressed in the currently used measuring procedure, but are accumulated regardless of the number of analyses. Other details and principles of MARC dating technique are published in Konečný et al. (2018).

Laser ablation inductively coupled plasma mass spectrometry (LA ICPMS) analysis for determination of Y and HREEs in garnet was performed in CEITEC, Masaryk University, Brno, Czech Republic by instrumentation consisting of laser ablation system UP213 (NewWaveResearch) and quadrupole ICP-MS Agilent 7500 ce. For details of the method see Petrík et al. (2019).

Results

Petrography and mineral chemistry

For dating and petrological study, we studied three samples of kyanite-bearing paragneiss: VV-29, VV-30 with abundant monazite and KO-7 poor in monazite. The samples are medium-grained rocks, which are strongly deformed and foliated. The deformed matrix consists mostly of plagioclase and biotite, with variable quartz, muscovite and flaky graphite. Sample VV-29 is unusual by its very low quartz content. Abundant subhedral plagioclase (59 vol. %) has basicity typically An_{36} containing more sodic domains with An_{20}. The rounded domains are irregularly found either within the basic plagioclases or at its rims. Porphyroblasts of garnet, kyanite (Fig. 2A–D) and biotite contain inclusions of rutile (Fig. 2A,B). Garnet porphyroblasts show mostly inclusion-free cores in contrast to rims with inclusions of plagioclase, quartz, biotite and muscovite/phengite; biotite and plagioclase often penetrating the garnet rim (Fig. 2D). Sample VV-30 is similar to VV-29, but differs by normal content of quartz (ca. 20 vol. %) and by the absence of kyanite. Plagioclase is anhedral, filled by small drop-like quartz, with basicity An_{36}, also containing sodic domains with An_{20}. Graphite is
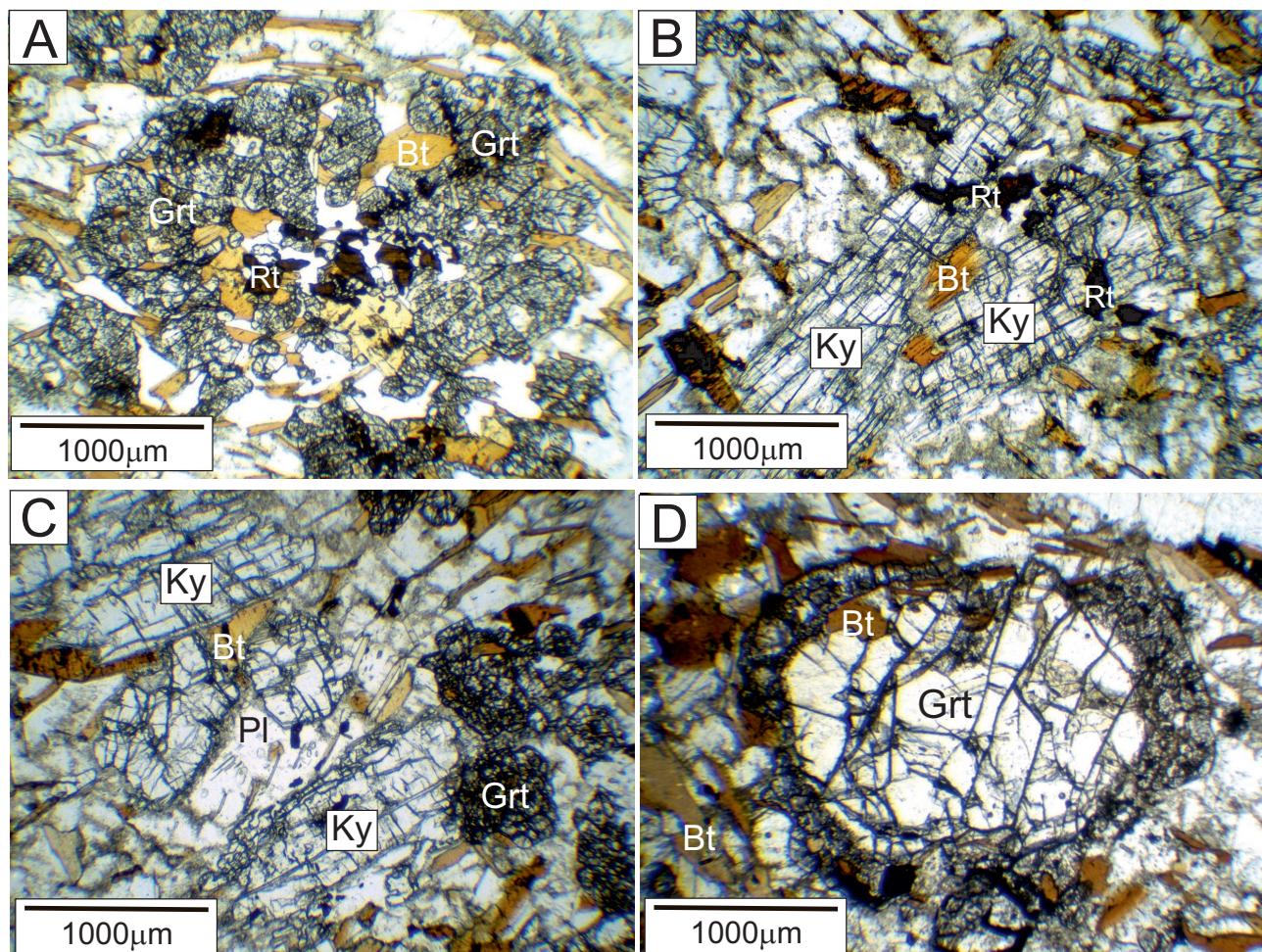
Fig. 2. Photomicrographs of paragneiss texture. **A, B** — Garnet (Grt), kyanite (Ky), biotite (Bt) and rutile (Rt), plane polarized transmitted light. **C** — Garnet (Grt), kyanite (Ky), biotite (Bt) and plagioclase (Pl), plane polarized light. **D** — Garnet porphyroblast with abundant inclusions in the rim, plane polarized transmitted light.

abundant, usually associated with biotite or rutile. Accessories are represented by numerous small zircons and monazite.

Garnet composition is illustrated by four X-ray maps and profiles (Figs. 3, 4): The inclusion-rich rims are distinct by their higher Ca and lower Mg contents, which is confirmed by convex shape of X (molar fraction) of pyrope profile with XPrp decreasing from 0.19 in centre to 0.14 in rims. The XGrs profiles are reciprocal, disturbed by late diffusional zones (Fig. 3A). Only the garnet with monazite 4 (Fig. 4C) shows undisturbed profile with XPrp rising from centre (0.15 to 0.19) followed by drop to 0.13 at rims with reciprocal rise of XGrs. The Ca-rich zones are porous, containing small plagioclases, muscovites and phengites. The maps show late zones of Ca penetrating the garnet but not following the brittle cracks often filled by chlorite. Yttrium was analysed by microprobe (profiles in Fig. 3) and Y+HREE by LA ICP MS (profiles in Fig. 4). Garnets in Fig. 3B and 4B show small peak in centres and more distinct peaks close to rims.

White mica is mostly muscovite (VV-29, Si/11O=3.1–3.2), small phengite (Si/11O=3.25–3.33) is commonly found as inclusions in Ca-rich garnet rims. *Biotite* forms red-brown porphyroblasts in the matrix, often replacing garnet (Fig. 4A, B) and kyanite as a consequence of resorption. Biotite composition in monazite-rich samples (VV-29, 30) is similar, with TiO_2=1.4–2 wt. %, and MgO=10–12 wt. %.

Representative analyses of garnet and white mica are shown in Tables 1–2, mineral abbreviations are according to Whitney & Evans (2010).

Monazite occurrence

Monazite was found in two textural positions, either occurring in the matrix or enclosed in garnet. The first one is larger, 50–100 μm in size, with poorly defined shape, the latter is typically rounded and smaller, 20–30 μm in size (Fig. 5A,B). Monazite in the matrix invariably undergoes extensive transformation to secondary coronas consisting of allanite, or REE-epidote and apatite, Th- and U-rich secondary phases (Fig. 5C–D, see also Fig. 10E–H). These coronas are usually larger than preserved monazite grains. The small enclosed
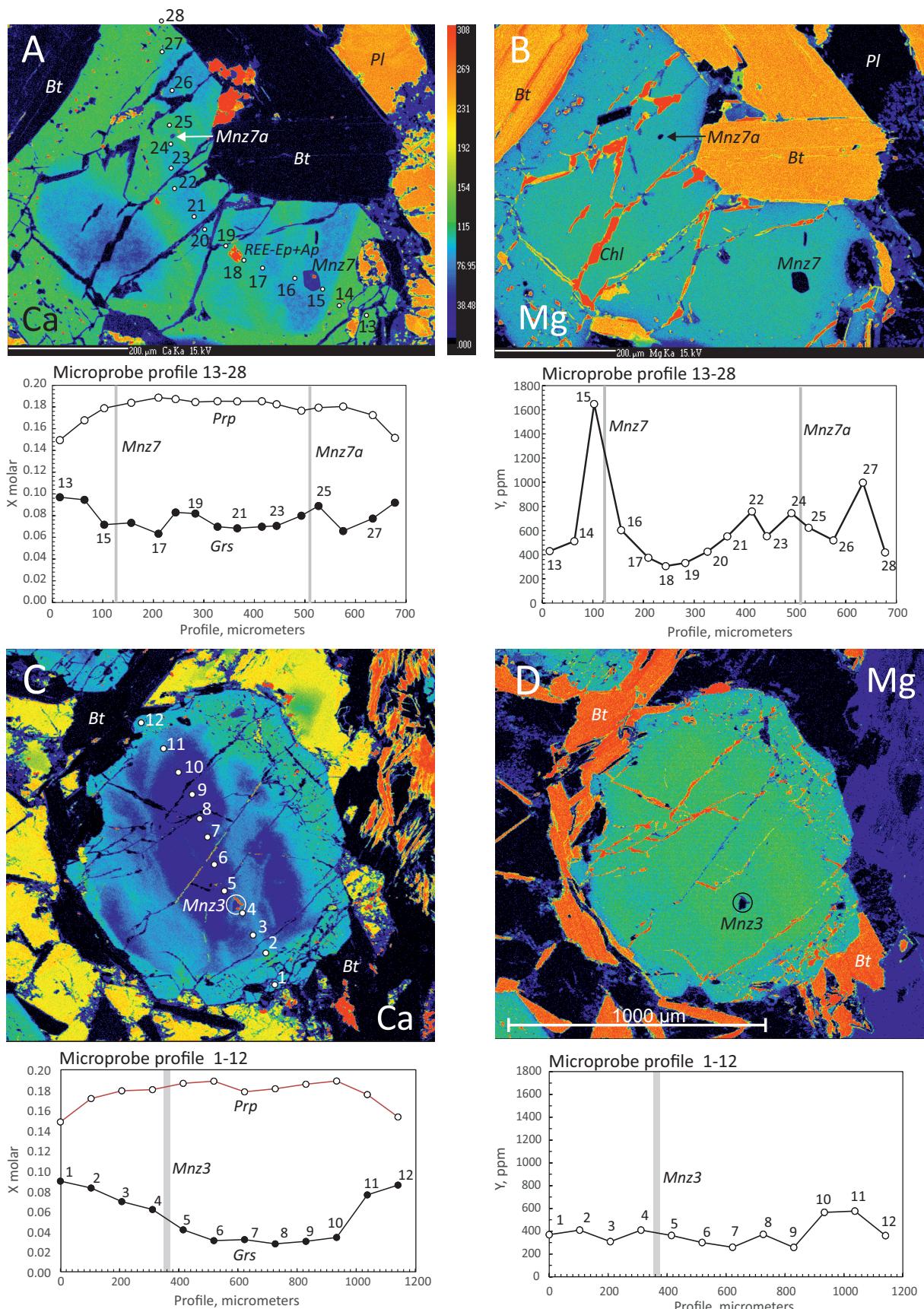
Fig. 3. X-ray maps of Mg and Ca in garnets containing monazite 7, 7a (**A**, **B**) and 3 (**C**, **D**) and microprobe profiles showing molar fractions X Prp, X Grs and Y, sample VV-29.
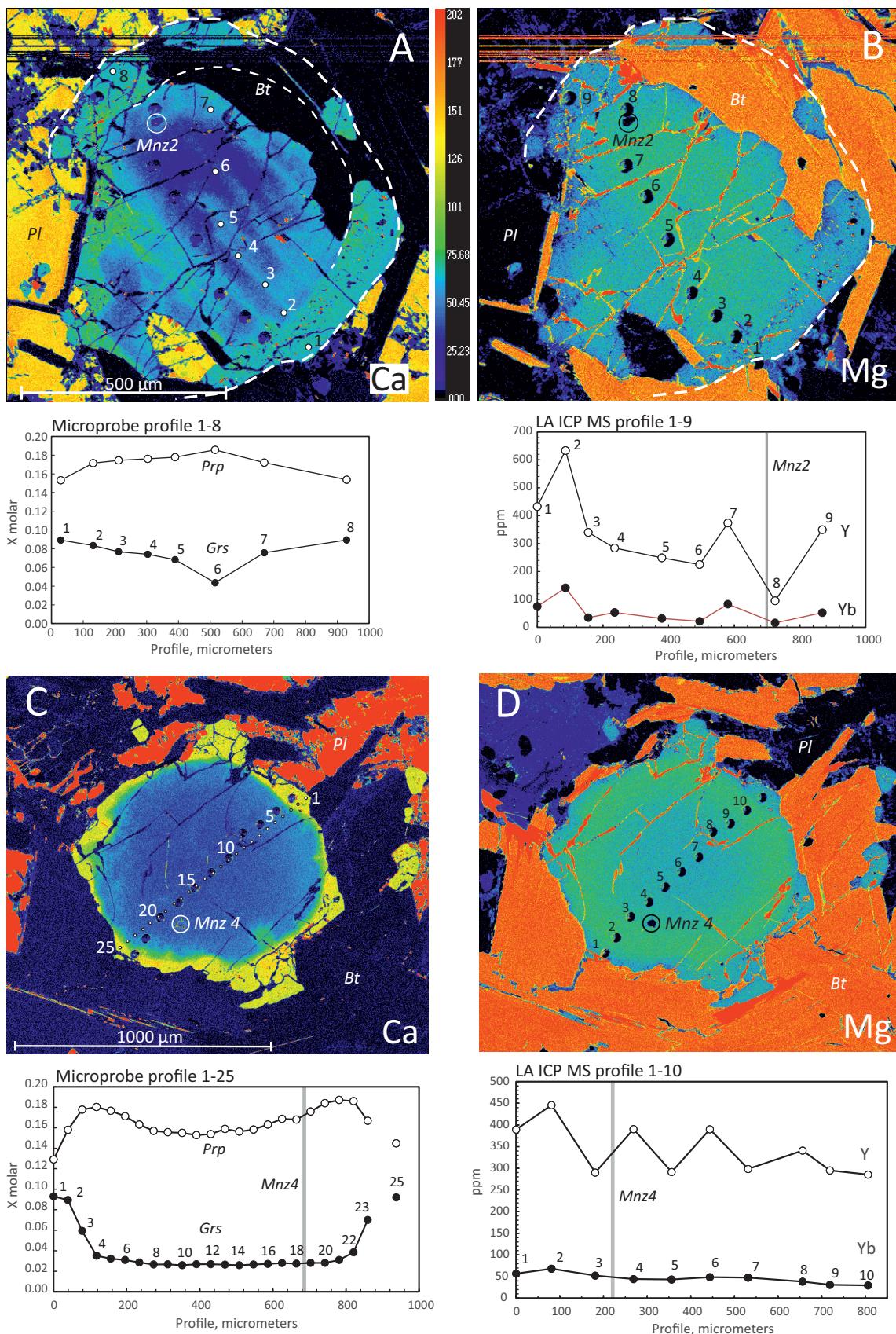
Fig. 4. X-ray maps of Mg and Ca in garnets containing monazite 2 (**A**, **B**), and 4 (**C**, **D**). Microprobe and LA ICP MS profiles show molar fractions of X Prp and X Grs, and concentrations of Yand Yb. Original outline of garnet is indicated in (A, B). Note the reversed orientation of the profile in (D), sample VV-29.

Table 1: Representative microprobe analyses of garnet.

Sample	VV-30	VV-30	VV-29	VV-29	VV-29	VV-29	VV-29	VV-29
Position	Grt core	Grt rim	Grt core	Grt rim	Grt edge	Grt rim	Grt rim	Grt rim
SiO_2	36.24	36.65	37.78	38.20	37.90	37.79	37.57	37.16
TiO_2	0.00	0.01	0.01	0.00	0.01	0.02	0.04	0.06
Al_2O_3	21.15	21.19	21.31	21.20	21.11	20.69	20.87	20.19
FeO	30.86	30.98	31.50	31.46	30.72	30.52	30.10	30.89
MnO	5.55	3.50	6.15	4.58	4.47	3.80	3.71	4.13
MgO	4.88	4.05	3.94	4.65	3.28	3.68	3.63	3.23
CaO	1.18	3.56	0.96	1.26	3.29	3.65	3.82	3.60
Y_2O_3	na	na	na	na	na	0.05	0.06	0.08
Total	99.86	99.93	101.66	101.36	100.79	100.23	99.86	99.46
12 O								
Si	2.919	2.942	2.986	3.002	3.009	3.015	3.005	3.007
Ti	0.000	0.000	0.001	0.000	0.001	0.001	0.002	0.004
Al	2.008	2.005	1.985	1.963	1.976	1.946	1.967	1.925
Fe	2.078	2.080	2.082	2.068	2.040	2.036	2.014	2.090
Mn	0.378	0.238	0.412	0.305	0.301	0.257	0.251	0.283
Mg	0.586	0.485	0.465	0.545	0.389	0.438	0.433	0.39
Ca	0.102	0.306	0.082	0.106	0.280	0.312	0.327	0.312
Y						0.002	0.003	0.003
Total	8.071	8.055	8.011	7.990	7.995	8.007	8.002	8.014
X_{Fe}	0.66	0.67	0.68	0.68	0.68	0.67	0.67	0.68
X_{Mg}	0.23	0.18	0.18	0.22	0.15	0.14	0.14	0.13
X_{Ca}	0.03	0.10	0.03	0.04	0.09	0.10	0.11	0.10
X_{Mn}	0.12	0.08	0.14	0.10	0.10	0.08	0.08	0.09

Table 2: Representative analyses of phengitic micas.

Sample	VV-30	VV-29	VV-29	VV-29	VV-29	VV-29	VV-29	VV-29
Position	Ph in matrix	Ph in Grt rim	Ph in Grt rim	Ph in Grt rim	Ph in Grt rim	Ph in Grt rim	Ph in Grt rim	Ph in Grt rim
SiO_2	47.186	48.747	47.046	50.12	47.49	48.10	50.64	48.90
TiO_2	0.024	0.126	0.064	0.09	0.05	0.15	0.01	0.16
Al_2O_3	28.855	28.549	31.052	30.94	29.89	30.77	27.84	26.98
FeO	2.482	3.549	2.573	2.55	2.70	2.06	3.66	3.73
MnO	0.003	0.139	0.088	0.18	0.10	0.10	0.16	0.08
MgO	2.785	2.606	2.998	3.48	2.59	2.02	2.96	3.74
CaO	0.022	0.108	0.043	0.05	0.07	0.02	0.12	0.14
Na_2O	0.167	0.194	0.280	0.22	0.21	0.26	0.18	0.22
K_2O	10.900	9.950	10.050	9.63	10.42	11.01	9.83	9.97
Cl	0.011	0.030	0.037	0.02	0.03	0.02	0.02	0.03
H_2Ocalc	4.464	4.468	4.472	4.52	4.47	4.48	4.49	4.46
Total	97.078	98.646	98.918	101.78	98.03	99.00	99.92	98.42
O=Cl	−0.003	−0.007	−0.008	0.00	−0.01	0.00	0.00	−0.01
Total	97.075	98.639	98.909	101.77	98.02	98.99	99.91	98.42
Si	3.267	3.313	3.182	3.263	3.244	3.247	3.382	3.336
Al^{IV}	0.733	0.687	0.818	0.737	0.756	0.753	0.618	0.664
X	4.000	4.000	4.000	4.000	4.000	4.000	4.000	4.000
Al^{VI}	1.622	1.600	1.658	1.638	1.650	1.696	1.573	1.505
Ti	0.001	0.006	0.003	0.004	0.003	0.007	0.000	0.008
Fe^{2+}	0.144	0.202	0.146	0.139	0.154	0.116	0.205	0.213
Mn	0.000	0.008	0.005	0.010	0.006	0.006	0.009	0.005
Mg	0.287	0.264	0.302	0.337	0.264	0.203	0.294	0.380
Y	2.055	2.080	2.116	2.128	2.077	2.028	2.083	2.112
Na	0.022	0.025	0.037	0.027	0.028	0.034	0.023	0.029
Ca	0.002	0.008	0.003	0.003	0.005	0.002	0.009	0.010
K	0.963	0.863	0.867	0.800	0.908	0.948	0.837	0.868
Z	0.992	0.901	0.912	0.831	0.941	0.984	0.869	0.907
Total	7.047	6.981	7.028	6.959	7.018	7.012	6.952	7.019
Cl	0.001	0.003	0.004	0.002	0.003	0.002	0.002	0.004
OH	1.999	1.997	1.996	1.998	1.997	1.998	1.998	1.996
Cations	7.047	6.981	7.028	6.959	7.018	7.012	6.952	7.019

(intact) monazites occur only in garnet outer zones, rarely, the breakdown products after monazite were found in garnet (Fig. 3A). In BSE images monazite shows no or weak zoning.

Monazite dating

Total 75 spot apparent individual ages were obtained from the two samples containing monazite. The data from both samples (VV-29: 60 points, VV-30: 15 points; Table 3) are interpreted together. Apparent ages yielded two distinct age groups: 330–400 Ma, and 450–524 Ma. The first group is represented by a homogeneous population, which gives a weighted average of 354.1±4.0 (MSWD=0.99). The latter population is less homogeneous giving a weighted average of 491.8±6.8 Ma and higher MSWD=1.4. Therefore, deconvolution was applied to this group, which resolved two ages: 485.3±6 (65 %) and 505±8 Ma (35 %) (Fig. 6).

The obtained ages, therefore, represent three populations, one of Carboniferous age, and two others with older, Ordovician and Cambrian ages. The Carboniferous ages represent 65 %, Ordovician 12 % and Cambrian 23 % of all points. With one significant exception all Carboniferous monazites are found in the matrix, commonly bordering garnet, the exception is a small monazite 7 (336–338 Ma), which occurs

in the garnet close to the rim (Fig. 3A, B). In the same garnet another monazite (7a) occurs which yielded the old age (515±28 Ma).

Monazite composition

In terms of minor elements (Ca, Si, Th, U) all analysed monazites from this sample show relatively monotonous composition with cheralite 6–10 mol. %, xenotime 3–6 mol. %, huttonite less than 2 mol. %, and corresponding 85–91 mol. % of monazite (Supplementary Table S1). The age populations overlap each other. Monazites follow a substitution trend to cheralite, with the Variscan age population slightly shifted to the huttonite trend (Fig. 7A). The same shift is seen also in Ca vs Si correlation. Carboniferous monazites also show a positive correlation of Th vs U, (Fig. 7B) with U reaching 0.04 apf (1.08 wt. % U) in contrast to the older monazites with U below 0.025 pfu (0.8 wt. % U). Seven points of the sample VV-30 do not show a consistent trend in these minor elements.

The REEs: Microprobe analyses provide reliable data for La to Dy, the heavier REEs are more scattered. Yttrium is used as a proxy for Ho, which has almost the same ionic radius. The REEs of the three age groups show small
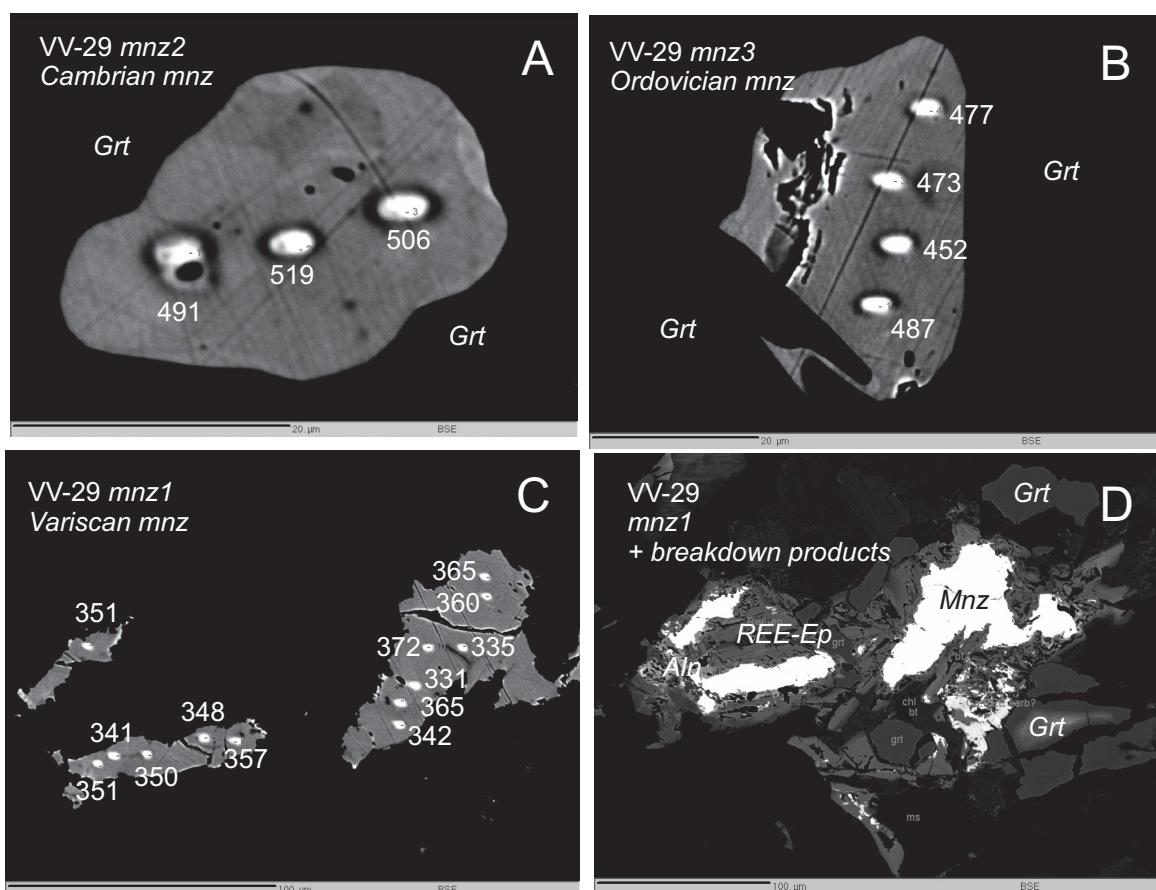
Fig. 5. BSE images of monazites of the three age groups: **A** — Cambrian; **B** — Ordovician; **C, D** — Variscan, (D) monazite with its breakdown products.

Table 3: Results of monazite dating, in wt. %. corr — values corrected according to MARC method

Sample	Point	Thcorr	U	Pb	Y	Ucorr	Pbcorr	Th 2σ	U 2σ	Pb 2σ	Age, Ma	2σ
VV-29	mnz1/1	2.676	0.453	0.079	1.423	0.4221	0.0634	0.0318	0.0128	0.0055	351	35
VV-29	mnz1/2	3.316	0.565	0.092	1.147	0.5269	0.0788	0.0365	0.0133	0.0056	351	29
VV-29	mnz1/3	3.103	0.493	0.081	0.968	0.4568	0.0697	0.0350	0.0130	0.0055	341	31
VV-29	mnz1/4	2.436	0.412	0.072	1.364	0.3834	0.0575	0.0300	0.0126	0.0055	350	38
VV-29	mnz1/5	2.587	0.419	0.075	1.368	0.3886	0.0598	0.0311	0.0127	0.0055	348	37
VV-29	mnz1/6	2.571	0.410	0.076	1.388	0.3800	0.0606	0.0312	0.0127	0.0056	357	38
VV-29	mnz1/7	3.420	0.387	0.086	1.379	0.3469	0.0695	0.0373	0.0126	0.0056	342	32
VV-29	mnz1/8	2.718	0.630	0.092	1.484	0.5981	0.0760	0.0319	0.0134	0.0055	365	31
VV-29	mnz1/9	3.681	0.643	0.101	1.517	0.6007	0.0831	0.0390	0.0135	0.0055	331	25
VV-29	mnz1/10	2.766	0.408	0.082	1.391	0.3757	0.0663	0.0325	0.0127	0.0055	372	36
VV-29	mnz1/11	2.605	0.414	0.072	1.380	0.3837	0.0575	0.0310	0.0125	0.0055	335	36
VV-29	mnz1/12	2.586	0.425	0.078	1.364	0.3950	0.0631	0.0308	0.0125	0.0055	365	36
VV-29	mnz1/13	2.651	0.430	0.079	1.394	0.3996	0.0634	0.0313	0.0125	0.0055	360	36
VV-29	mnz2/1	4.397	0.303	0.123	0.509	0.2515	0.1150	0.0442	0.0120	0.0056	491	29
VV-29	mnz2/2	3.773	0.236	0.114	0.898	0.1917	0.1027	0.0400	0.0120	0.0057	519	35
VV-29	mnz2/3	4.430	0.219	0.127	1.000	0.1674	0.1132	0.0449	0.0119	0.0057	506	32
VV-29	mnz3/1	3.946	0.463	0.138	1.900	0.4169	0.1160	0.0413	0.0129	0.0058	487	30
VV-29	mnz3/2	3.883	0.425	0.131	1.869	0.3804	0.1088	0.0408	0.0128	0.0057	473	30
VV-29	mnz3/3	3.424	0.380	0.111	1.721	0.3404	0.0918	0.0374	0.0125	0.0057	452	33
VV-29	mnz3/4	3.676	0.431	0.127	1.831	0.3880	0.1057	0.0393	0.0128	0.0057	477	31
VV-29	mnz3/5	4.126	0.600	0.154	2.231	0.5388	0.1278	0.0386	0.0134	0.0059	484	22
VV-29	mnz3/7	3.908	0.467	0.137	1.835	0.4120	0.1146	0.0373	0.0129	0.0058	486	25
VV-29	mnz4/1	3.674	0.389	0.124	1.903	0.3466	0.1025	0.0390	0.0124	0.0057	475	32
VV-29	mnz4/2	2.906	0.589	0.124	1.507	0.5557	0.1076	0.0332	0.0133	0.0056	508	32
VV-29	mnz4/3	2.112	0.587	0.107	1.434	0.5620	0.0930	0.0277	0.0134	0.0057	524	39
VV-29	mnz4/4	3.986	0.485	0.143	2.112	0.4391	0.1187	0.0305	0.0131	0.0059	488	29
VV-29	mnz4/5	3.883	0.530	0.149	2.126	0.4847	0.1245	0.0302	0.0133	0.0059	507	29
VV-29	mnz4/6	1.411	0.386	0.069	1.222	0.3593	0.0545	0.0219	0.0127	0.0055	471	47
VV-29	mnz4/7	3.606	0.539	0.131	1.542	0.4853	0.1120	0.0350	0.0129	0.0057	481	24
VV-29	mnz4/8	3.237	0.455	0.121	1.548	0.4075	0.1022	0.0333	0.0129	0.0057	498	28
VV-29	mnz5/1	2.514	0.578	0.085	2.026	0.5484	0.0634	0.0303	0.0132	0.0055	331	33
VV-29	mnz5/2	3.132	0.714	0.111	2.388	0.6774	0.0843	0.0352	0.0140	0.0057	354	28
VV-29	mnz5/3	2.621	0.536	0.091	1.798	0.5056	0.0722	0.0315	0.0132	0.0056	379	34
VV-29	mnz5/4	2.695	0.570	0.087	1.736	0.5384	0.0685	0.0319	0.0134	0.0056	345	32
VV-29	mnz5/5	2.717	0.571	0.089	1.742	0.5395	0.0703	0.0321	0.0134	0.0056	352	32
VV-29	mnz5/6	2.580	0.566	0.085	1.764	0.5219	0.0647	0.0293	0.0133	0.0056	339	29
VV-29	mnz6/1	3.096	0.550	0.095	1.480	0.5143	0.0783	0.0346	0.0131	0.0055	368	30
VV-29	mnz6/2	3.384	0.813	0.119	2.186	0.7732	0.0941	0.0373	0.0145	0.0057	357	25
VV-29	mnz7/2	3.773	0.587	0.103	1.712	0.5436	0.0830	0.0298	0.0135	0.0058	336	27
VV-29	mnz7/3	3.471	0.596	0.101	1.665	0.5419	0.0805	0.0347	0.0133	0.0057	345	24
VV-29	mnz7/4	3.645	0.499	0.097	1.624	0.4460	0.0761	0.0357	0.0131	0.0057	335	25
VV-29	mnz 8/1	3.706	0.384	0.132	1.745	0.3413	0.1118	0.0296	0.0128	0.0059	516	33
VV-29	mnz8/2	3.408	0.379	0.113	1.706	0.3391	0.0932	0.0285	0.0127	0.0058	461	34
VV-29	mnz9/2	4.500	0.978	0.136	1.665	0.9254	0.1155	0.0323	0.0153	0.0059	345	20
VV-29	mnz9/3	3.323	0.765	0.104	1.418	0.7268	0.0876	0.0282	0.0143	0.0057	346	26
VV-29	mnz10/1	3.759	0.425	0.126	1.467	0.3728	0.1074	0.0363	0.0128	0.0058	481	26
VV-29	mnz11/1	3.802	0.995	0.128	1.733	0.9257	0.1067	0.0362	0.0144	0.0057	351	19
VV-29	mnz14-1	3.563	0.635	0.149	2.448	0.5789	0.1213	0.0353	0.0135	0.0059	496	24
VV-29	mnz14/2	3.535	0.632	0.149	2.377	0.5759	0.1218	0.0351	0.0135	0.0059	501	24
VV-29	mnz14/3	3.894	0.691	0.157	2.556	0.6298	0.1275	0.0373	0.0137	0.0059	478	22
VV-29	mnz14/4	3.544	0.630	0.155	2.505	0.5743	0.1264	0.0347	0.0133	0.0058	519	24
VV-29	mnz15/2	4.407	0.789	0.136	1.999	0.7188	0.1109	0.0403	0.0141	0.0058	368	19
VV-29	mnz16/2	4.495	0.736	0.125	1.709	0.6670	0.1029	0.0409	0.0139	0.0058	346	19
VV-29	mnz16/3	4.489	0.741	0.126	1.717	0.6717	0.1034	0.0408	0.0139	0.0057	347	19
VV-29	mnz17/2	2.581	0.374	0.075	1.313	0.3362	0.0586	0.0291	0.0126	0.0055	357	34
VV-29	mnz17/3	2.781	0.434	0.084	1.436	0.3915	0.0662	0.0304	0.0128	0.0056	365	31
VV-29	mnz17/4	2.743	0.425	0.078	1.428	0.3841	0.0607	0.0301	0.0127	0.0055	341	31
VV-29	mnz17/5	3.068	0.787	0.110	1.647	0.7309	0.0907	0.0322	0.0140	0.0057	373	23
VV-29	mnz17/7	2.570	0.402	0.076	1.347	0.3631	0.0596	0.0291	0.0127	0.0055	356	33
VV-29	mnz17/8	2.118	0.511	0.079	1.416	0.4734	0.0624	0.0263	0.0130	0.0055	382	34

Table 3 (continued)

Sample	Point	Thcorr	U	Pb	Y	Ucorr	Pbcorr	Th 2σ	U 2σ	Pb 2σ	Age, Ma	2σ
VV-30	mnz1/1	5.191	0.765	0.190	1.511	0.7051	0.1702	0.0505	0.0143	0.0059	506	22
VV-30	mnz2/1	1.534	0.469	0.078	1.150	0.4516	0.0672	0.0233	0.0128	0.0055	497	49
VV-30	mnz3/1	4.589	0.618	0.124	1.835	0.5645	0.1012	0.0460	0.0136	0.0057	353	23
VV-30	mnz3/2	3.561	0.457	0.095	1.453	0.4159	0.0778	0.0384	0.0128	0.0056	355	30
VV-30	mnz3/3	4.546	0.542	0.119	1.582	0.4888	0.0987	0.0457	0.0133	0.0057	360	24
VV-30	mnz3/4	3.543	0.661	0.110	1.989	0.6201	0.0876	0.0383	0.0138	0.0057	353	27
VV-30	mnz4/1	0.921	0.758	0.074	1.779	0.7475	0.0581	0.0188	0.0141	0.0055	388	42
VV-30	mnz4/2	0.950	0.759	0.072	1.814	0.7477	0.0556	0.0191	0.0141	0.0055	369	42
VV-30	mnz4/3	1.053	0.868	0.083	1.893	0.8557	0.0653	0.0198	0.0146	0.0056	382	37
VV-30	mnz4/4	0.989	1.043	0.087	2.006	1.0318	0.0677	0.0194	0.0155	0.0056	351	33
VV-30	mnz4/5	1.049	0.888	0.080	1.866	0.8761	0.0630	0.0199	0.0147	0.0055	363	36
VV-30	mnz4/6	1.065	0.780	0.080	1.809	0.7671	0.0629	0.0199	0.0142	0.0055	395	40
VV-30	mnz4/7	1.015	0.783	0.078	1.691	0.7707	0.0629	0.0195	0.0143	0.0055	400	40
VV-30	mnz4/8	0.992	0.773	0.074	1.762	0.7617	0.0579	0.0193	0.0142	0.0055	375	41
VV-30	mnz5/1	2.946	1.078	0.119	1.939	1.0439	0.0982	0.0339	0.0157	0.0057	348	24
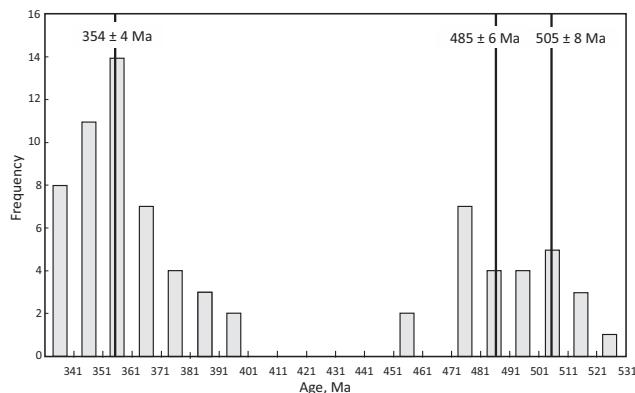
Fig. 6. Histogram of individual ages showing three age groups Cambrian, Ordovician and Early Carboniferous (Variscan). Weighted average ages are also shown.

differences (Fig. 8A–C). The Carboniferous and Ordovician monazites form distinct groups which differ in their Y_N and Eu anomalies. The former group (Fig. 8A) has the least negative Eu, i.e. the highest Eu/Eu* values with the average of 0.243 and lowest Y_N with the average of 7477. The Ordovician group (Fig. 8B) is also homogeneous with more negative Eu anomalies (average Eu/Eu*=0.124). The oldest group (Fig. 8C, 6 points) is heterogeneous with variable both Eu anomalies (0.22–0.04) and Y_N contents (5000–10000).

Comparing monazites from two samples (VV-29 and VV-30; Fig. 9), shows that they differ in La, Sm, Nd contents, Carboniferous monazites in VV-30 having higher La and lower Sm and Nd than in VV-29. Old monazites of both samples have the lowest La and highest Sm and Nd, i.e. less steep slope of LREE. Distributions of U, Th and Y were obtained by X-ray mapping for Variscan monazites (Fig. 10). They are different for the monazite 7 enclosed in garnet compared to the monazite 9 from the matrix. The first (Fig. 10A–D) has increased U and Th in irregular patches in the centre enclosed by indistinct thin depleted rim. Yttrium loosely correlates with U in the centre but does not form the thin rim. Matrix monazite 9 (Fig. 10E–H) is strongly attacked showing corona of epidote and allanite with scattered spots of secondary concentrations of Th, U and Y. Yttrium is concentrated to one part of the monazite loosely correlating with U. The breakdown clearly involves high mobility of all three mapped elements. Yttrium concentrations in points 2, 4 were used in garnet – monazite thermometry, see below.

Garnet Y and REE contents

Garnets containing monazite were analysed for major elements including Y_2O_3 by microprobe along profiles and two of them also by laser ablation (LA ICP MS) method for trace elements (Table 4). Garnets with monazites 2, 3, 4 and 7 were mapped by X-rays (Figs. 3, 4), REE and Y profiles were obtained by laser ablation for Grt/Mnz2 and Grt/Mnz4. Comparison of microprobe and LA analyses shows that microprobe analyses, which are close to the detection limit, overestimate Y in garnet approximately by up to 40 %. However, the patterns of Y distribution along the profiles are well seen. Garnets with monazites 2 and 7 show weak central peaks and marked secondary peaks (Figs. 3B, 4B), garnets with monazites 3 and 4 have more flat profiles with less distinct peaks (Figs. 3D, 4D). Normalized HREEs have convex upward patterns of two analysed garnets with no or only slight increase between Ho and Lu (Fig. 11). Grt/Mnz2 shows fan-like patterns from Gd to Lu (A). The LREEs are mostly below detection limit except the points 1, 2, 6, and 8, which are probably contaminated by small monazites. Grt/Mnz4 (B) has also convex upward patterns which are more homogeneous and generally lower. Both garnets probably have small negative Eu anomalies.

Y-in-garnet and monazite thermometer

Partitioning of Y between garnet and coexisting monazite ca be used as geothermometer (Pyle et al. 2001; Hacker et al.

2019). Monazite was found included in four garnets in sample VV-29. Two garnets, which have profiles analysed for HREE and Y by LA ICP MS, were used for thermometry using the equation of Hacker et al. (2019). Laser ablation analyses give 570 °C for Grt/Mnz2 and 601 °C for Grt/Mnz4. Garnet containing monazite 7 (Fig. 10A) and monazite 7a of two
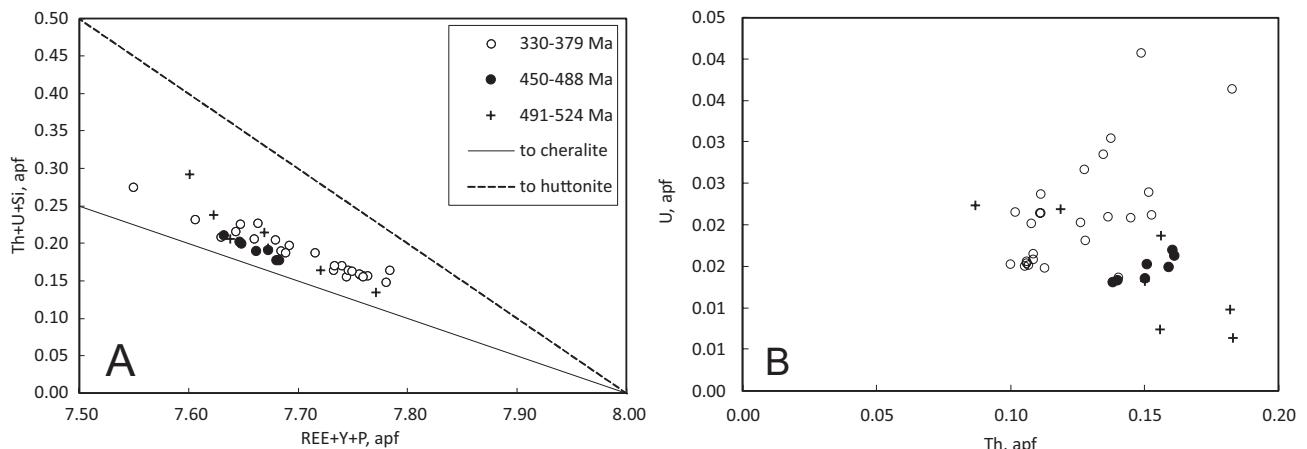
Fig. 7. A — Mnz substitution relations; **B** — U vs. Th relations; divided according the age groups.
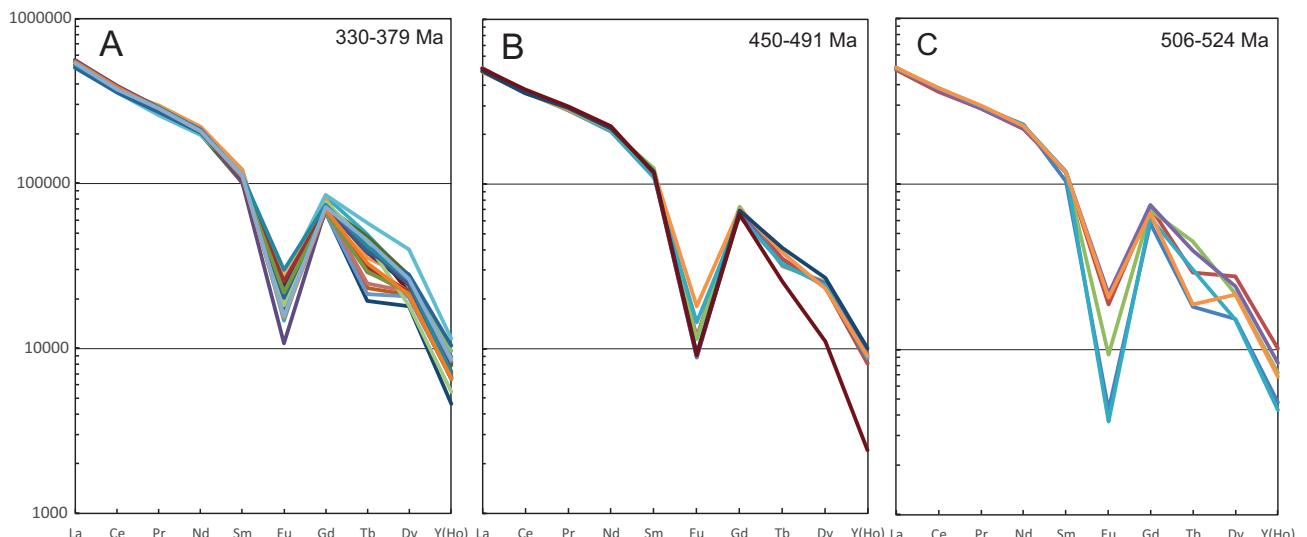
Fig. 8. Monazite REE patterns of the three age groups, sample VV-29.
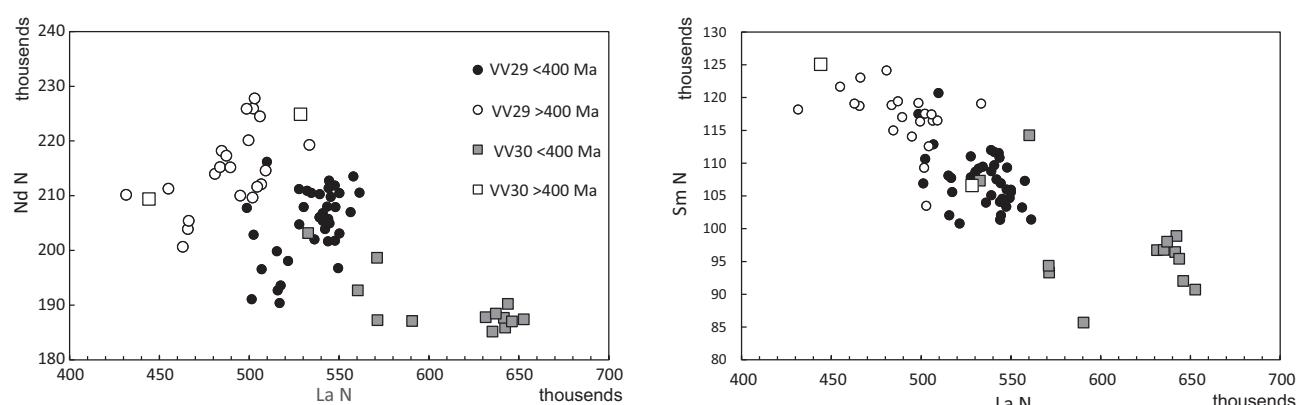
Fig. 9. Comparison of LREE correlation in older (>400 Ma) and younger (<400 Ma) monazites.
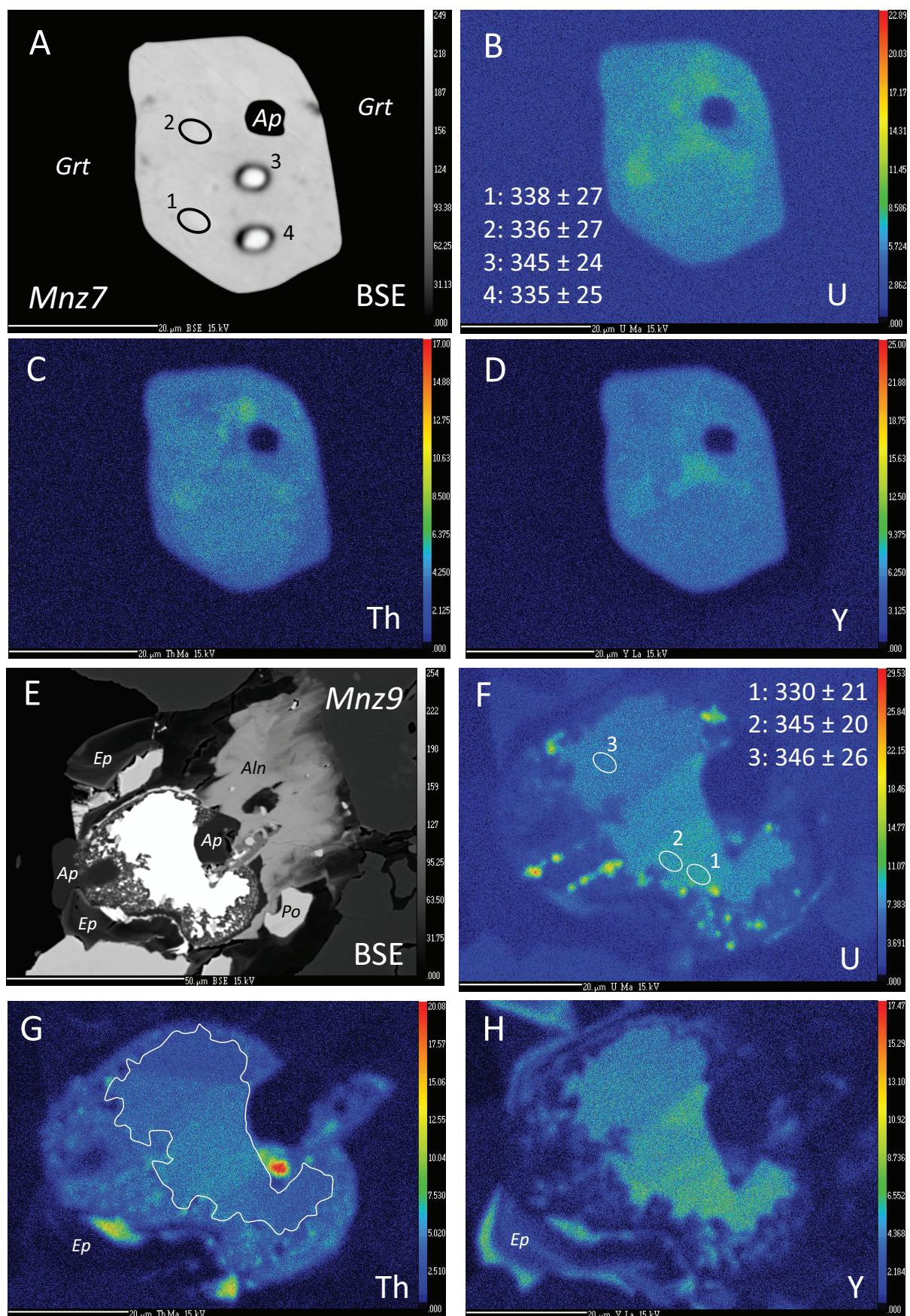
Fig. 10. X-ray maps (U, Th, Y) of monazite 7, enclosed in garnet (**A–D**) and monazite 9 found in matrix (**E–H**).

Table 4: LA ICP MS analyses of garnets with monazites 2, 4 (ppm). DL — detection limit.

G/M2	an 1	an 2	an 3	an 4	an 5	an 6	an 7	an 8	an 9	DL
Sc	150	131	190	187	207	187	108	64	179	6
Ti	8847	23	37	27	17	1025	2666	3368	145	5
Cr	286	434	186	105	128	231	131	118	377	8
Y	433	634	340	284	249	225	374	95	350	0.1
Zr	5.3	5.8	4.1	2.3	3.5	2.9	2.3	0.5	8.4	0.1
Th	0.6	0.4	<	<	<	1.1	<	<	<	0.3
U	<	<	<	<	<	<	<	<	<	0.4
La	1.8	2.2	<	<	<	0.6	<	0.3	<	0.1
Ce	2.7	3.9	<	<	<	0.6	0.1	0.8	<	0.1
Pr	0.4	0.4	<	<	<	<	<	<	<	0.3
Nd	1.4		0.7	<	<	0.8	<	<	<	0.7
Sm		0.9	<	<	<	<	<	<	1.5	0.8
Eu	0.5		0.2	<	<	<	0.2	<	<	0.2
Gd	3.5	5.9	3.8	5.0	4.9	6.9	3.7	2.7	5.5	1
Tb	3.2	3.3	2.9	2.5	2.3	2.5	2.5	0.7	3.1	0.2
Dy	46	57	34	37	27	26	39	12	52	0.6
Ho	15	24	9.5	9.2	8.7	7.6	12	3.8	13	0.1
Er	51	98	30	43	28	22	48	13	44	0.1
Tm	8.1	18	4.3	6.9	3.8	2.6	9.4	2.1	6.2	0.1
Yb	75	142	35	53	31	21	83	16	52	0.6
Lu	12	21	3.9	9.5	3.3	2.6	14	2.2	6.5	0.1

G/M4	an 1	an 2	an 3	an 4	an 5	an 6	an 7	an 8	an 9	an 10
Sc	107	177	203	236	229	221	210	215	217	221
Ti	170	57	55	64	59	54	59	32	34	47
Cr	8	695	405	319	160	204	177	149	151	298
Y	389	446	290	390	291	390	298	341	295	286
Zr	4.4	4.5	5.0	5.8	2.6	2.9	3.5	4.0	8.2	5.4
Th	<	<	<	<	<	<	<	0.3	<	<
U	<	<	<	<	<	<	<	<	<	<
La	0.2	<	<	<	<	<	<	0.1	<	<
Ce	0.9	<	<	<	<	<	0.2	0.2	<	<
Pr	<	<	<	<	<	<	<	<	<	<
Nd	<	<	<	<	<	<	<	<	<	<
Sm	0.9	0.8	1.5	<	<	1.0	<	<	1.2	<
Eu	0.4	0.2	<	0.2	<	<	<	<	<	<
Gd	6.3	10	6.0	4.8	3.8	3.4	3.5	5.6	4.9	7.7
Tb	2.9	3.8	2.9	3.2	2.0	2.1	2.3	2.7	2.8	3.6
Dy	47	46	35	41	30	33	31	35	36	39
Ho	14	15	11	13	10	10	11	12	11	11
Er	54	53	43	43	39	45	44	41	31	32
Tm	8.0	9.0	6.1	5.6	5.9	6.0	7.2	5.1	4.6	4.6
Yb	57	68	52	44	43	49	48	38	31	30
Lu	6.9	10	7.1	5.9	6.6	7.1	7.8	4.8	4.1	4.5

different ages gives the same temperatures for both monazites (557–568 for monazite 7 and 565–575 for monazite 7a), calculated from microprobe analyses of both minerals.

Phase equilibrium modelling and geothermobarometry

The *P–T* sections were calculated using Perple_X thermodynamic software (Connolly 2005: version 6.8.6) with the internally consistent thermodynamic dataset (hp11ver.dat) of Holland & Powell (2011). Solid-solution models for omphacite, garnet, white mica, biotite, ilmenite (White et al. 2014), and plagioclase (Newton et al. 1980) were used, as available

from the Perple_X datafile (solution_model.dat). The bulk rock composition used in the calculations for peak-pressure and retrogression stages was constrained by whole-rock analysis of sample VV-29 (SiO_2 46.91, TiO_2 1.3, Al_2O_3 22.45, FeO 8.43, MnO 0.24, MgO 5.48, CaO 2.46, Na_2O 3.37, K_2O 4.3, H_2O 1.5).

Pseudosection (Fig. 12A, B) was calculated with controlled oxygen fugacity, log fO_2=−19. On cooling these redox conditions cover a wide range, from reducing at 700 °C (below FMQ buffer), which is in accord with presence of graphite) to oxidising (above HM buffer), which stabilise epidote below 520 °C at 9 kbars. The low H_2O content was chosen to avoid
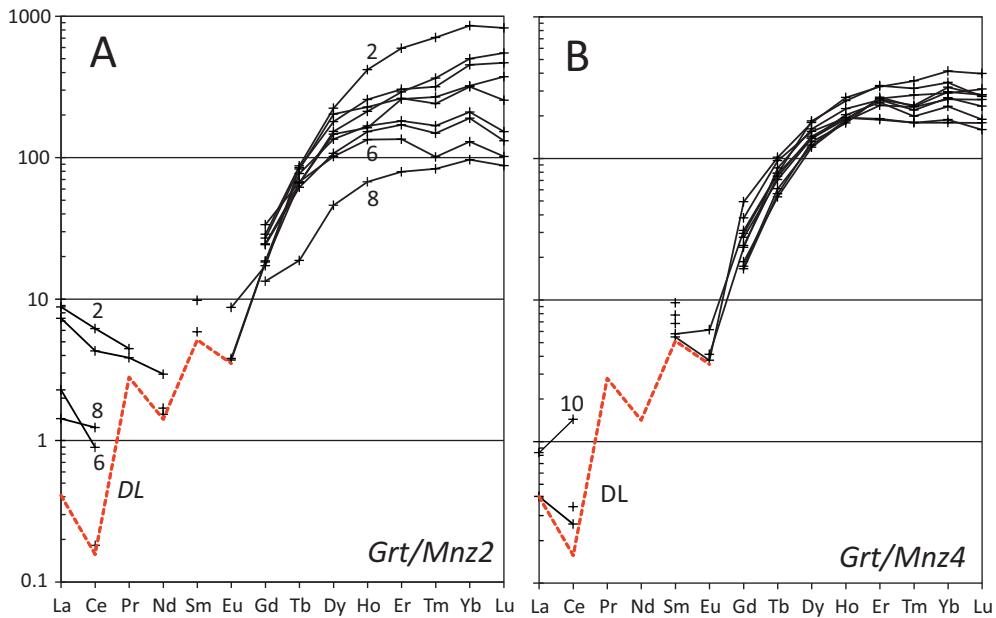
Fig. 11. The REE patterns of garnets with monazites 2 (**A**) and 4 (**B**). DL — detection limit. Points 2, 6, 8 (A) and 10 (B) were probably contaminated by small monazites.
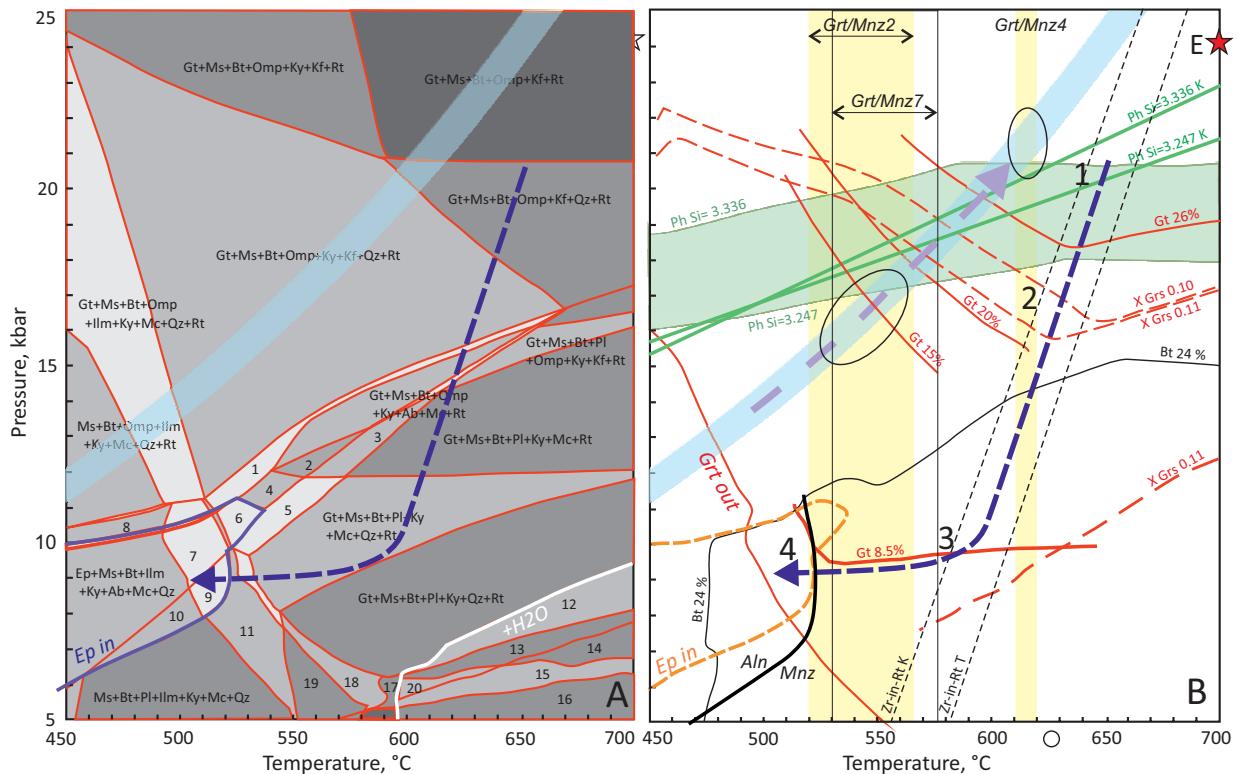
Fig. 12. A — Pseudosection of sample VV-29; **B** — Suggested *P–T* path, for 1–4 see text. The prograde path (light violet) follows a subduction geotherm according to Penniston-Dorland et al. (2015). The star with E indicates peak *P–T* conditions of eclogite and metaultramafite hosted by gneisses in the northern Veporic unit (Janák et al. 2009, 2020). For other details see the text. Field numbers: 1: Gt, Ms, Bt, Omp, Ky, Ab, Mc, Qz, Rt; 2: Gt, Ms, Bt, Ky, Ab, Mc, Rt; 3: Gt, Ms, Bt, Pl, Ky, Ab, Mc, Rt; 4: Gt, Bt, Ms, Ky, Ab, Mc, Qz, Rt; 5: Gt, Bt, Ms, Pl, Ky, Ab, Mc, Qz, Rt; 6: Ep, Gt, Ms, Bt, Ky, Ab, Mc, Qz, Rt; 7: Ep, Gt, Ms, Bt, Ilm, Ky, Ab, Mc, Qz; 8: Ms, Bt, Omp, Ilm, Ky, Ab, Mc, Qz; 9: Ep, Gt, Ms, Bt, Pl, Ilm, Ky, Mc, Qz; 10: Ep, Ms, Bt, Pl, Ilm, Ky, Mc, Qz; 11: Gt, Ms, Bt, Pl, Ilm, Ky, Mc, Qz; 12: Gt, Ms, Bt, Pl, Ky, Qz, Rt, H2O; 13: Gt, Bt, Pl, Ky, Qz, Rt, H2O; 14: Gt, Bt, Pl, Sill, Qz, Rt, H2O; 15: Gt, Bt, Pl, Ilm, Sill, Qz, Rt, H2O; 16: Gt, Bt, Pl, Ilm, Sill, Qz, H2O; 17: Gt, Bt, Pl, Ilm, Ky, Qz, H2O; 18: Gt, Ms, Bt, Pl, Ilm, Ky, Qz, Rt; 19: Gt, Ms, Bt, Pl, Ilm, Ky, Qz; 20: Gt, Bt, Pl, Ilm, Ky, Qz, Rt, H2O.

the generation of too abundant muscovite content during retrogression. The allanite–monazite boundary calculated by Spear (2010) for similar Al_2O_3 and CaO contents (Al_2O_3=20.7, CaO=2.17 wt. %), is superimposed on the pseudosection, at this fO_2 it coincides with the appearance of epidote. The reconstruction of the *P–T* path experienced by the studied paragneiss is based on textural relations of monazite–garnet and garnet core–rim, their compositions, phengite composition, and Zr in rutile thermometry. The peak conditions are based on the intersection of maximum Si in phengite (3.336) with univariant line of Zr-in-Rt thermometry (Fig. 12B, point 1). Isopleths of phengite Si/11O agree well with empirical phengite barometry (Kamzolkin et al. 2016, green lines marked with K). They intersect with two univariant lines (calculated by two calibrations of Zr-in rutile thermometer according to Tomkins et al. 2007 and Kohn 2020, dashed lines T and K) at maximal pressure and temperature of 21 kbars and 650 °C. The *P–T* path then follows retrogression (point 2) along the univariant lines down to 9 kbars, corresponding to 8.5 vol. % of garnet, which is the measured modal content in the sample (point 3). The *P–T* path then continues by cooling to the monazite–allanite boundary and epidote-in curve at 520 °C. At 480 °C the cooling path would approach the 24 vol. % of biotite isopleth, corresponding to the measured modal amount (point 4). Garnet compositions provide additional insight to the *P–T* evolution. X-ray maps of four garnets (Figs. 3, 4) containing monazite show: (1) distinct Ca rims overgrowing cores, (2) extensive Ca diffusion from the rims to cores along linear zones. The highest preserved CaO contents of the rims (X Grs=0.1–0.11) intersect with decompression path at two pressures: 16–17 kbars (point 2) and at 8–9 kbars. The former intersection is favoured because the rims commonly enclose high-pressure phengites, which is not true for the low-pressure intersection. It is inferred that Ca-rims overgrew garnet cores at 16–17 kbars. The MgO contents of both cores and rims are too low and do not give realistic intersections. This is likely a result of diffusional modification by heating above 550 °C during prograde stage when Mg diffuses faster than Ca (Carlson 2006; Caddick et al. 2010; Young & Kylander-Clark 2015).

Monazites included in garnet always occur in the cores (Figs. 3, 4), the Y-in-Grt/Mnz2 and 4 temperatures (calculated by the equation of Hacker et al. 2019) are shown by yellow columns. Their position in cores precludes the columns intersection with retrogression path and suggests monazite entrapment during the prograde stage. In Fig. 12A,B a prograde *P–T* path following subduction-related geotherm (Penniston-Dorland et al. 2015) is shown in light violet colour. Calculated Grt/Mnz2 temperatures (520–570 °C) intersect with the prograde *P–T* trajectory at 15–17 kbars, those of monazite 4 (610–620 °C) at 21–22 kbars (ellipses). While monazite 2 would coexist with 15–20 % of garnet, monazite 4 with 26 % of garnet. Later appearance of higher temperature monazite 4 coexisting with the highest garnet content would explain its lower and more homogenous Y-REE contents (Fig. 11).

Discussion

According to the *P–T* path suggested in Fig. 12A,B monazites 2 and 4 were trapped during prograde metamorphic stage. However, both these monazites are old (Ordovician to Cambrian, Table 3). The Ordovician monazites have the same age as abundant metagranites and orthogneisses found in the northern Veporic unit and probably record the coeval metamorphism or they are inherited from magmatic source. The Cambrian monazite is most probably inherited and its age refers to metasedimentary protolith. Only the youngest monazite 7 (Fig. 10) enclosed in garnet core dates the Variscan metamorphism. The pair Grt/Mnz7 yields temperature 530–577 °C, slightly higher than monazite 2, because it was calculated from microprobe analyses. These temperatures, along with position in the garnet core, indicate that monazite (338 Ma, n=4) dates prograde metamorphism, actually below the peak of metamorphism. The Variscan metamorphism is confirmed by matrix monazites, which yielded the average age of 354 Ma. It is, therefore, possible that matrix monazites nucleated earlier than those included by garnet. Similar age relations between older matrix monazites and younger monazites included in garnet were found in the Western Gneiss Region of Scandinavian Caledonides (Holder et al. 2015). The extensive Ca diffusion revealed by X-ray maps in our samples is interpreted as a result of concentration gradient between the garnet cores and rims. Downhill diffusion of Ca across garnet stepped profile at 650 °C and 5 kbars in length of 1000 μm in 10 Ma was successfully modelled by Caddick et al. (2010). We infer that the garnet rims in our samples had originally higher CaO contents but this would have little effect on calculated XGrs isopleths. The inference that monazite was enclosed by garnet during prograde stage is in accord with Y profiles of garnets (Figs. 3B, 4B), which may be interpreted as a diffusion-limited uptake during rising temperature producing central peak and annular maxima (secondary peaks) according to Skora et al. (2006) and Moore et al. (2013).

The dominant Carboniferous monazite population (353±5 Ma) indicates a strong Variscan metamorphic event which overprinted possibly earlier metamorphic assemblages and produced the new metamorphic monazite. Similar Variscan age (347±1.7 Ma) was also obtained on monazites from nearby granitic orthogneisses (Veľký Zelený Potok, south of the Hron river, Ondrejka et al. 2012). Monazite from the latter locality is also similar to our samples by extensive development of secondary coronas, described in detail by above authors.

It should be noted that garnet contains also a reacted monazite (now REE-epidote+apatite+REE carbonate) located in a Ca-enriched zone connecting Ca-rich rims of garnet (Fig. 3A). The low-temperature (ca. 520 °C) of monazite breakdown process was probably caused by retrogression affecting these garnet rims penetrated by biotite and chlorite. The monazite REE patterns showing negative Eu anomalies (Fig. 8A) are commonly used to argue that it was in equilibrium with plagioclase (e.g. Zhu & O'Nions 1999), although as

shown by Petrík et al. (2019) it can also be inherited from the whole rock REEs. The first explanation would be possible in the case of our samples supposing that plagioclase remained metastable due to reluctant response to HP metamorphism (Young & Kylander-Clark 2015). In fact, prograde *P–T* conditions in our investigated paragneisses are less than those (25 kbars; 700 °C) recorded by eclogites and metaultramafic rocks in the same area (Janák et al. 2007, 2020). It is worth noting that no Alpine age was recorded by monazite in our studied rocks indicating that the degree of Alpine reworking in the northern Veporic basement has not reached the temperature of monazite resetting or a new growth. We therefore attribute the monazite breakdown to retrogression stage of Variscan metamorphism.

Conclusions

The investigated kyanite-bearing paragneisses of the northern Veporic unit reached *P–T* conditions of 21 kbars and 650 °C. Dating of monazite using Th–U–Pb method yielded Carboniferous (354±4 Ma) age, reflecting prograde Variscan metamorphism. This is deduced from temperatures of 520–620 °C calculated from monazite equilibrated with garnet and monazite position in the garnet cores. Transformation of monazite to allanite indicates cooling to ca 520 °C during retrogression at oxidizing conditions, which stabilised epidote.

Besides the Variscan, inherited monazite recorded also Ordovician and Cambrian ages in accord with existing zircon ages.

The results of this study confirm that high-pressure metamorphism was recorded by several rock types (eclogite, metaultramafite, paragneiss) in the pre-Alpine basement of the Veporic Unit and strongly support its Variscan age.

References

Bezák V., Jacko S., Janák M., Ledru P., Petrík I. & Vozárová A. 1997: Main Hercynian lithotectonic units of the Western Carpathians. In: Grecula P., Hovorka D. & Putiš M. (Eds.): Geological Evolution of the Western Carpathians. *Mineralia Slovaca – Monographs*, Bratislava, 261–268.

Biely A., Beňuška P., Bezák V., Bujnovský A., Halouzka R., Ivanička J., Kohút M., Klinec A., Lukáčik E., Maglay J., Miko O., Pulec M., Putiš M. & Vozár J. 1992: Geological map of the Nízke Tatry Mts. 1:50,000. *GÚDŠ*, Bratislava.

Caddick M.J., Konopásek J. & Thompson A.B. 2010: Preservation of garnet growth zoning and the duration of prograde metamorphism. *Journal of Petrology* 51, 2327–2347. https://doi.org/10.1093/petrology/egq059

Carlson W.D. 2006: Rates of Fe, Mg, Mn, and Ca diffusion in garnet. *American Mineralogist* 91, 1–11. https://doi.org/10.2138/am.2006.2043

Catlos E., Gilley L.D. & Harrison T.M. 2002: Interpretation of monazite ages obtained via in situ analysis. *Chemical Geology* 188, 193–215. https://doi.org/10.1016/S0009-2541(02)00099-2

Connolly J.A.D. 2005: Computation of phase-equilibria by linear programming: A tool for geodynamic modeling and its application to subduction zone decarbonation. *Earth and Planetary Science Letters* 236, 524–541. https://doi.org/10.1016/j.epsl.2005.04.033

Engi M. 2017: Petrochronology based on REE-minerals: Monazite, allanite, xenotime, apatite. In: Kohn M.J., Engi M. & Lanari P. (Eds.): Petrochonology: Methods and applications. *Reviews in Mineralogy and Geochemistry* 83, 365–418. https://doi.org/10.2138/rmg.2017.83.12

Faryad S.W., Ivan P. & Jacko S. 2005: Metamorphic petrology of metabasites from the Branisko and Čierna hora mountains (Western Carpathiansm Slovakia*). Geologica Carpathica* 56, 3–16.

Faryad S.W., Ivan P. & Jedlička R. 2020: Pre-Alpine high-pressure metamorphism in the Gemer unit: mineral textures and their geodynamic implications for Variscan Orogeny in the Western Carpathians. *International Journal of Earth Sciences* 10, 1547–1564. https://doi.org/10.1007/s00531-020-01856-2

Finger F., Broska I., Roberts M.P. & Schermaier A. 1998: Replacement of primary monazite by apatite–allanite–epidote coronas in an amphibolite facies granite gneiss from the eastern Alps. *American Mineralogist* 83, 248–258. https://doi.org/10.2138/am-1998-3-408

Gaab A.S., Poller U., Janák M. & Todt W. 2006: Zircon U–Pb geochronology and isotopic characterization of the pre-Mesozoic basement of the Northern Veporic Unit (Central Western Carpathians, Slovakia). *Schweizerische Mineralogische und Petrographische Mitteilungen* 85, 69–85.

Gieré R., Rumble D., Günther D., Connolly J. & Caddick M. J. 2011: Correlation of growth and breakdown of major and accessory minerals in metapelites from Campolungo, Central Alps. *Journal of Petrology* 52, 2293–2334. https://doi.org/10.1093/petrology/egr043

Hacker B., Kylander-Clark A. & Holder R. 2019: REE partitioning between monazite and garnet: Implications for petrochronology. *Journal of Metamorphic Geology* 37, 227–237. https://doi.org/10.1111/jmg.12458

Hermann, J. & Rubatto, D. 2003: Relating zircon and monazite domains to garnet growth zones: age and duration of granulite facies metamorphism in the Val Malenco lower crust. *Journal of Metamorphic Geology* 21, 833–852. https://doi.org/10.1046/j.1525-1314.2003.00484.x

Holder R.M., Hacker B.R., Kylander-Clark A.R.C. & Cottle J.M. 2015: Monazite trace-element and isotopic signatures of (ultra) high-pressure metamorphism: Examples from the Western gneiss Region, Norway. *Chemical Geology* 409, 99–111. https://doi.org/10.1016/j.chemgeo.2015.04.021

Holland T.J.B. & Powell R. 2011: An improved and extended internally consistent thermodynamic dataset for phases of petrological interest, involving a new equation of state for solids. *Journal of Metamorphic Geology* 29, 333–383. https://doi.org/10.1111/j.1525-1314.2010.00923.x

Hovorka D. & Méres Š. 1990: Clinopyroxene-garnet metabasites from the Tribeč Mts. (Central Slovakia). *Mineralia Slovaca*, 22, 533–538.

Hovorka D., Méres Š. & Caňo F. 1992: Petrology of the garnet-clinopyroxene metabasites from the Malá Fatra Mts. *Mineralia Slovaca*, 24, 45–52.

Hovorka D., Méres Š. & Ivan P. 1994: Pre-Alpine Western Carpathians basement complexes: lithology and geodynamic setting.

Mitteilungen der Österreichischen Geologischen Gesellschaft 86, 33–44.

Hovorka D., Ivan P. & Méres Š. 1997: Leptyno-amphibolite complex of the Western Carpathians: its definition, extent and genetical problems. In: Grecula P., Hovorka D. & Putiš M. (Eds.): Geological Evolution of the Western Carpathians. *Mineralia Slovaca – Monographs*, Bratislava, 269–280.

Ivan P., Hovorka D. & Méres Š. 1996: Gabbroid rocks – a newly found member of the leptyno-amphibolite complex of the Western Carpathians. *Slovak Geological Magazine* 3–4, 199–203.

Janák M. & Lupták B. 1997: Pressure–temperature conditions of high-grade metamorphism and migmatization in the Malá Fatra crystalline complex, the Western Carpathians. *Geologica Carpathica* 48, 287–302.

Janák M., O'Brien P.J., Hurai V. & Reutel C. 1996: Metamorphic evolution and fluid composition of garnet–clinopyroxene amphibolites from the Tatra Mountains, Western Carpathians. *Lithos* 39, 57–79. https://doi.org/10.1016/S0024-4937(96)00019-9

Janák M., Plašienka D., Frey M., Cosca M., Schmidt S.Th., Lupták B. & Méres Š. 2001: Cretaceous evolution of a metamorphic core complex, the Veporic unit, Western Carpathians (Slovakia): P–T conditions and in situ ⁴⁰Ar/³⁹Ar UV laser probe dating of metapelites. *Journal of Metamorphic Geology* 19, 197–216. https://doi.org/10.1046/j.0263-4929.2000.00304.x

Janák M., Finger F., Plašienka D., Petrík I., Humer B., Méres Š. & Lupták B. 2002: Variscan high P–T recrystallization of Ordovician granitoids in the Veporic unit (Nízke Tatry Mountains, Western Carpathians): new petrological and geochronological data. *Geolines*, 14, 38–39.

Janák M., Méres Š. & Ivan P. 2007: Petrology and metamorphic P–T conditions of eclogites from the northern Veporic Unit (Western Carpathians, Slovakia). *Geologica Carpathica* 58, 121–131.

Janák M., Mikuš T., Pitoňák P. & Spišiak J. 2009: Eclogites overprinted in the granulite facies from the Ďumbier crystalline complex (Low Tatra Mountains, Western Carpathians). *Geologica Carpathica* 60, 193–204.

Janák M., Méres Š. & Medaris G. 2020: Eclogite facies metaultramafite from the Veporic Unit (Western Carpathians, Slovakia). *Geologica Carpathica* 71, 209–220. https://doi.org/10.31577/GeolCarp.71.3.1

Jeřábek P., Janák M., Faryad S.W., Finger F. & Konečný P. 2008a: Polymetamorphic evolution of pelitic schists and evidence for Permian low-pressure metamorphism in the Vepor Unit, West Carpathians. *Journal of Metamorphic Geology* 26, 465–485. https://doi.org/10.1111/j.1525-1314.2008.00771.x

Jeřábek P., Faryad S. W., Schulmann K., Lexa O. & Tajčmanová L. 2008b: Alpine burial and heterogeneous exhumation of Variscan crust in the West Carpathians: Insight from thermodynamic and argon diffusion modeling. *Journal of the Geological Society* 165, 479–498. https://doi.org/10.1144/0016-76492006-165

Jeřábek P., Lexa O., Schulmann K. & Plašienka D. 2012: Inverse ductile thinning via lower crustal flow and fold-induced doming in the West Carpathian Eo-Alpine collisional wedge. *Tectonics* 31, TC5002. https://doi.org/10.1029/2012TC003097

Kamzolkin V.A., Ivanov S.D. & Konilov A.N. 2016: Empirical phengite geobarometer: background, calibration, and application. *Geology of Ore Deposits* 58, 613–622. https://doi.org/10.1134/S1075701516080092

Klinec A. 1966: On the problems of structure and origin of the Vepor crystalline complex (in Slovak). *Západné Karpaty* 6, 7–28.

Kohn M.J. 2020: A refined zirconium-in-rutile thermometer. *American Minerlogist* 105, 963-971. https://doi.org/10.2138/am-2020-7091

Kohn M.J., Wieland M.S., Parkinson C.D. & Upreti B.N. 2005: Five generations of monazite in Langtang gneisses: implications for chronology of Himalayan metamorphic core. *Journal of Metamorphic Geology* 23, 399–406. https://doi.org/10.1111/j.1525-1314.2005.00584.x

Konečný P., Kusiak M.A. & Dunkley D.J. 2018: Improving U–Th–Pb electron microprobe dating using monazite age references. *Chemical Geology* 484, 22–35. https://doi.org/10.1016/j.chemgeo.2018.02.014

Kráľ J., Frank W. & Bezák V. 1996: Hornblende ⁴⁰Ar/³⁹Ar spectra from the hornblende-bearing rocks of the Veporic unit. *Mineralia Slovaca* 28, 501–513.

Krenn E., Janák M., Finger F., Broska I. & Konečný P. 2009: Two types of metamorphic monazite with contrasting La/Nd, Th, and Y signatures in an ultrahigh-pressure metapelite from the Pohorje Mountains, Slovenia: Indications for pressure-dependent REE exchange between apatite and monazite? *American Mineralogist* 89, 1323–1329. https://doi.org/10.2138/am.2009.2981

Lupták B., Janák M., Plašienka D. & Schmidt S. Th. 2003: Alpine low-grade metamorphism in the Veporic unit, Western Carpathians: phyllosilicates composition and crystallinity data. *Geologica Carpathica* 54, 367–375.

Majka J., Be'eri-Shlevin Y., Gee D.G., Ladenberger A., Claesson S., Konečný P. & Klonowska I. 2012: Multiple monazite growth in the Åreskutan migmatites: evidence for a polymetamorphic Late Ordovician to Late Silurian evolution in the Seve Nappe Complex of the west-central Jämtland, Sweden. *Journal of Geosciences* 57, 3–23. https://doi.org/10.3190/jgeosci.112

Méres Š., Hovorka D. & Ivan P. 1996: Gabbroids within the Veporic Unit of the Nízke Tatry Mts. (Western Carpathians). *Mineralia Slovaca* 28, 38–44 (in Slovak with English resumé).

Moore S.J., Carlson W.D. & Hesse M.A. 2013: Origins of yttrium and rare earth element distribution in metamorphic garnet. *Journal of Metamorphic Geology* 31, 663–689. https://doi.org/10.1111/jmg.12039

Moussallam Y., Schneider D.A., Janák M., Thöni M. & Holm D.K. 2012: Heterogeneous extrusion and exhumation of deep-crustal Variscan assembly: Geochronology of the Western Tatra Mountains, northern Slovakia. *Lithos* 144, 88–108. https://doi.org/10.1016/j.lithos.2012.03.025

Newton R.C., Charlu T.V. & Kleppa O.J. 1980: Thermochemistry of high structural state plagioclases. *Geochimica et Cosmochimica Acta* 44, 933–941.

Ondrejka M., Uher P., Putiš M., Broska I., Bačík P., Konečný P. & Schmiedt I. 2012: Two-stage breakdown of monazite by post-magmatic and metamorphic fluids: An example from the Veporic orthogneiss, Western Carpathians, Slovakia. *Lithos* 142–143, 245–255. https://doi.org/10.1016/j.lithos.2012.03.012

Penniston-Dorland S.C., Kohn M.J. & Manning C.E. 2015: The global range of subduction zone thermal structures from exhumed blueschists and eclogites: Rocks are hotter than models. *Earth and Planetary Science Letters* 428, 243–254. https://doi.org/10.1016/j.epsl.2015.07.031

Petrík I., Janák M., Froitzheim N., Georgiev N., Yoshida K., Sasinková V. Konečný P. & Milovská S. 2016: Triassic to Early Jurassic (c. 200 Ma) UHP metamorphism in the Central Rhodopes: evidence from U–Pb–Th dating of monazite in diamond-bearing gneiss from Chepelare (Bulgaria). *Journal of Metamorphic Geology* 34, 265–291. https://doi.org/10.1111/jmg.12181

Petrík I., Janák M. & Vaculovič T. 2017: Ordovician magmatites of the northern Veporic unit: polymetamorphic S-type granites. In: Open Congress of Slovak and Czech Geological Societies, Vysoké Tatry 2017. *SGS and ČGS*, 1–2 (in Slovak).

Petrík I., Janák M., Klonowska I., Majka J., Froitzheim N., Yoshida K., Sasinková V., Konečný P. & Vaculovič T. 2019: Monazite behaviour during metamorphic evolution of a diamond-bearing gneiss: a case study from the Seve Nappe Complex, Scandinavian Caledonides. *Journal of Petrology* 60, 1773–1796. https://doi.org/10.1093/petrology/egz051

Plašienka D. 2018. Continuity and episodicity in the Early Alpine tectonic evolution of the Western Carpathians: how large-scale processes are expressed by the orogenic architecture and rock record data. *Tectonics* 37, 2029–2079. https://doi.org/ 10.1029/2017TC004779

Plašienka D., Grecula P., Putiš M., Hovorka D. & Kováč M. 1997: Evolution and structure of the Western Carpathians: an overview. In: Grecula P., Hovorka D. & Putiš M. (Eds.): Geological Evolution of the Western Carpathians. *Mineralia Slovaca – Monographs*, Bratislava, 1–24.

Putiš M., Filová I., Korikovsky S.P., Kotov A.B. & Madarás J. 1997: Layered metaigneous complex of the Veporic basement with features of the Variscan and Alpine thrust tectonics (the Western Carpathians). In: Grecula P., Hovorka D. & Putiš M. (Eds.): Geological Evolution of the Western Carpathians. *Mineralia Slovaca – Monographs*, Bratislava, 176–196.

Putiš M., Sergeev S., Ondrejka M., Larionov A., Siman P., Spišiak J., Uher P. & Paderin I. 2008: Cambrian-Ordovician metaigneous rocks associated with Cadomian fragments in the West-Carpathian basement dated by SHRIMP on zircons: a record from the Gondwana active margin setting. *Geologica Carpathica* 59, 3–18.

Pyle J.M., Spear F.S., Rudnick R.L. & McDonough W.F. 2001: Monazite-xenotime-garnet equilibrium in metapelites and a new monazite-garnet thermometer. *Journal of Petrology* 42, 2083–2107. https://doi.org/10.1093/petrology/42.11.2083

Skora S., Baumgartner L.P., Mahlen N.J., Johnson C.M., Pilet S. & Hellebrand E. 2006: Diffusion-limited REE uptake by eclogite garnets and its consequences for Lu–Hf and Sm-Nd geochronology. *Contributions to Mineralogy and Petrology* 152, 703–720. https://doi.org/10.1007/s00410-006-0128-x

Spear F.S. 2010: Monazite-allanite phase relations in metapelites. *Chemical Geology* 279, 55–62. https://doi.org/10.1016/j.chemgeo.2010.10.004

Spear F.S. & Pyle J.M. 2002: Apatite, monazite and xenotime in metamorphic rocks. *Reviews in Mineralogy* 48, 293–335. https://doi.org/10.1515/9781501509636-010

Terry M.P., Robinson P., Hamilton M.A. & Jercinovic M. J. 2000: Monazite geochronology of UHP and HP metamorphism, deformation, and exhumation, Nordoyane, Western Gneiss Region, Norway. *American Mineralogist* 85, 1651–1664. https://doi.org/10.2138/am-2000-11-1208

Tomkins H. S., Powell R. & Ellis D. 2007: The pressure dependence of the zirconium-in-rutile thermometer. *Journal of Metamorphic Geology* 25, 703–713. https://doi.org/10.1111/j.1525-1314.2007.00724.x

Uher P., Broska I., Krzeminska E., Ondrejka M., Mikuš T. & Vaculovič T. 2019: Titanite composition and SHRIMP U–Pb dating as indicators of post-magmatic tectono-thermal activity: Variscan I-type tonalites to granodiorites, the Western Carpathians. *Geologica Carpathica* 70, 449–470.

Vojtko R., Králiková S., Jeřábek P., Schuster R., Danišík M., Fügenschuh B., Minár J. & Madarás J. 2016: Geochronological evidence for the Alpine tectono–thermal evolution of the Veporic unit (Western Carpathians, Slovakia). *Tectonophysics* 666, 48–65. https://doi.org/10.1016/j.tecto.2015.10.014

White R.W., Powell R., Holland T.J.B., Johnson T.E. & Green E.C.R. 2014: New mineral activity–composition relations for thermodynamic calculations in metapelitic systems. *Journal of Metamorphic Geology* 32, 261–286. https://doi.org/10.1111/jmg.12071

Whitney D.L. & Evans B.W. 2010: Abbreviations for names of rock-forming minerals. *American Mineralogist* 95, 185–187.

Young D.J & Kylander-Clark A.R.C. 2015: Does continental crust transform during eclogite facies metamorphism? *Journal of Metamorphic Geology* 33, 331–357. https://doi.org/10.1111/jmg.12123

Zhu X. K. & O'Nions R. K. 1999: Monazite chemical composition: some implications for monazite geochronology. *Contributions to Mineralogy and Petrology* 137, 351–363. https://doi.org/10.1007/s004100050555

Supplement

Table S1: Complete monazite microprobe analyses, structural formulae (per 16 O) and molar fractions of monazite, huttonite, cheralite and xenotime.

Sample	VV-29	VV-29	VV-29	VV-29	VV-29	VV-29	VV-29	VV-29	VV-29	VV-29	VV-29	VV-29
Grain	mnz1/1	mnz1/2	mnz1/3	mnz1/4	mnz1/5	mnz1/6	mnz1/7	mnz1/8	mnz1/9	mnz1/10	mnz1/11	mnz1/12
	Fig. 5C	Fig. 5C	Fig. 5C	Fig. 5C	Fig. 5C	Fig. 5C	Fig. 5C	Fig. 5C	Fig. 5C	Fig. 5C	Fig. 5C	Fig. 5C
Age, Ma	350.9	351.2	340.6	349.7	348.1	356.8	342.2	365.2	330.9	372.2	334.8	365.0
P_2O_5	29.709	29.089	29.032	29.149	29.244	29.263	29.192	29.030	28.854	29.523	29.367	29.342
PbO	0.066	0.082	0.072	0.059	0.062	0.063	0.072	0.079	0.087	0.069	0.060	0.065
ThO_2	3.046	3.774	3.531	2.772	2.943	2.925	3.892	3.093	4.189	3.148	2.965	2.942
UO_2	0.473	0.591	0.512	0.430	0.436	0.426	0.387	0.673	0.674	0.421	0.430	0.443
Y_2O_3	1.807	1.456	1.229	1.732	1.738	1.763	1.751	1.884	1.927	1.766	1.752	1.732
La_2O_3	15.608	15.512	16.002	15.779	15.705	15.616	15.262	16.101	15.381	15.717	15.583	15.465
Ce_2O_3	28.695	27.952	28.353	28.921	28.764	28.641	27.917	29.227	27.550	28.613	28.617	28.818
Pr_2O_3	3.175	3.119	3.181	3.179	3.251	3.279	3.247	3.232	3.191	3.220	3.260	3.266
Nd_2O_3	11.682	11.428	11.800	11.632	11.708	11.757	11.655	11.635	11.165	11.490	11.494	11.621
Sm_2O_3	1.810	1.995	1.916	1.892	1.846	1.910	1.949	1.810	1.857	1.952	1.992	1.877
Eu_2O_3	0.144	0.122	0.118	0.187	0.139	0.190	0.182	0.072	0.164	0.103	0.146	0.147
Gd_2O_3	1.662	1.825	1.580	1.553	1.612	1.681	1.752	1.634	1.693	1.643	1.599	1.577
Tb_2O_3	0.106	0.187	0.083	0.092	0.100	0.139	0.198	0.176	0.124	0.142	0.137	0.126
Dy_2O_3	0.639	0.532	0.525	0.605	0.613	0.641	0.633	0.725	0.653	0.616	0.593	0.627
Ho_2O_3	0.054	0.052	0.026	0.064	0.019	0.036	0.016	0.076	0.079	0.051	0.008	0.044
Er_2O_3	0.390	0.328	0.330	0.403	0.338	0.356	0.344	0.413	0.354	0.368	0.393	0.370
Tm_2O_3	0.113	0.106	0.101	0.111	0.069	0.058	0.070	0.111	0.113	0.116	0.099	0.117
Yb_2O_3	0.156	0.103	0.110	0.185	0.135	0.156	0.104	0.116	0.165	0.078	0.159	0.174
Lu_2O_3	0.101	0.075	0.084	0.106	0.076	0.128	0.046	0.066	0.117	0.103	0.124	0.049
FeO	0.161	0.081	0.116	0.081	0.178	0.177	0.137	0.109	0.090	0.067	0.022	0.145
SO_3	0.011	0.021	0.023	0.009	0.017	0.003	0.019	0.012	0.019	0.025	0.023	0.017
CaO	0.798	0.912	0.814	0.679	0.750	0.720	0.896	0.654	0.925	0.687	0.656	0.691
SrO	0.015	0.021	0.009	0.024	0.013	0.014	0.013	0.026	0.018	0.030	0.014	0.016
SiO_2	0.248	0.295	0.259	0.205	0.229	0.226	0.274	0.180	0.318	0.225	0.218	0.211
Total	100.667	99.659	99.804	99.845	99.984	100.165	100.007	101.131	99.706	100.170	99.708	99.881
P	3.936	3.912	3.910	3.915	3.918	3.917	3.912	3.883	3.890	3.935	3.933	3.930
Si	0.039	0.047	0.041	0.032	0.036	0.036	0.043	0.028	0.051	0.035	0.034	0.033
Total T	3.975	3.959	3.951	3.948	3.955	3.952	3.955	3.911	3.941	3.971	3.967	3.963
Ca	0.134	0.155	0.139	0.115	0.127	0.122	0.152	0.111	0.158	0.116	0.111	0.117
Th	0.108	0.136	0.128	0.100	0.106	0.105	0.140	0.111	0.152	0.113	0.107	0.106
U	0.016	0.021	0.018	0.015	0.015	0.015	0.014	0.024	0.024	0.015	0.015	0.016
Pb	0.003	0.004	0.003	0.003	0.003	0.003	0.003	0.003	0.004	0.003	0.003	0.003
La	0.901	0.909	0.939	0.923	0.917	0.911	0.891	0.938	0.903	0.913	0.909	0.902
Ce	1.644	1.626	1.651	1.680	1.667	1.658	1.618	1.690	1.606	1.649	1.657	1.669
Pr	0.181	0.181	0.184	0.184	0.187	0.189	0.187	0.186	0.185	0.185	0.188	0.188
Nd	0.653	0.648	0.670	0.659	0.662	0.664	0.659	0.656	0.635	0.646	0.649	0.657
Sm	0.098	0.109	0.105	0.103	0.101	0.104	0.106	0.099	0.102	0.106	0.109	0.102
Eu	0.008	0.007	0.006	0.010	0.008	0.010	0.010	0.004	0.009	0.006	0.008	0.008
Gd	0.086	0.096	0.083	0.082	0.085	0.088	0.092	0.086	0.089	0.086	0.084	0.083
Tb	0.005	0.010	0.004	0.005	0.005	0.007	0.010	0.009	0.007	0.007	0.007	0.007
Dy	0.032	0.027	0.027	0.031	0.031	0.033	0.032	0.037	0.033	0.031	0.030	0.032
Ho	0.003	0.003	0.001	0.003	0.001	0.002	0.001	0.004	0.004	0.003	0.000	0.002
Er	0.019	0.016	0.016	0.020	0.017	0.018	0.017	0.020	0.018	0.018	0.020	0.018
Tm	0.006	0.005	0.005	0.005	0.003	0.003	0.003	0.005	0.006	0.006	0.005	0.006
Yb	0.007	0.005	0.005	0.009	0.006	0.008	0.005	0.006	0.008	0.004	0.008	0.008
Lu	0.005	0.004	0.004	0.005	0.004	0.006	0.002	0.003	0.006	0.005	0.006	0.002
Y	0.150	0.123	0.104	0.146	0.146	0.148	0.147	0.158	0.163	0.148	0.148	0.146
Total cat.	8.034	8.043	8.045	8.047	8.045	8.045	8.045	8.062	8.052	8.028	8.030	8.035
X_{LREE}	0.857	0.852	0.869	0.868	0.865	0.864	0.849	0.861	0.837	0.864	0.866	0.866
X_{HREE}	0.040	0.041	0.036	0.039	0.037	0.040	0.040	0.041	0.041	0.039	0.039	0.039
X_{hut}	0.000	0.001	0.003	0.001	0.000	0.000	0.001	0.007	0.005	0.004	0.003	0.002
X_{cher}	0.066	0.076	0.068	0.056	0.062	0.060	0.074	0.053	0.077	0.057	0.055	0.058
X_{xno}	0.037	0.030	0.025	0.036	0.036	0.036	0.036	0.038	0.040	0.036	0.036	0.036

Table S1 (continued)

Sample	VV-29	VV-29	VV-29	VV-29	VV-29	VV-29	VV-29	VV-29	VV-29	VV-29	VV-29	VV-29
Grain	mnz1/13	mnz2/1	mnz2/2	mnz2/3	mnz3/1	mnz3/2	mnz3/3	mnz3/4	mnz4/1	mnz4/2	mnz4/3	mnz5/1
	Fig. 5C	Fig. 5A	Fig. 5A	Fig. 5A	Fig. 5B	Fig. 5B	Fig. 5B	Fig. 5B				
Age, Ma	359.8	491.0	519.4	506.3	487.0	473.1	452.0	476.6	475.4	507.7	524.1	331.3
P_2O_5	29.341	28.888	29.047	28.720	29.519	29.463	29.603	29.454	29.539	29.526	29.382	29.646
PbO	0.066	0.120	0.107	0.119	0.123	0.115	0.097	0.112	0.108	0.113	0.097	0.067
ThO_2	3.016	5.003	4.293	5.041	4.490	4.419	3.896	4.183	4.181	3.307	2.403	2.860
UO_2	0.448	0.276	0.210	0.181	0.465	0.423	0.379	0.432	0.386	0.624	0.633	0.617
Y_2O_3	1.771	0.646	1.140	1.269	2.413	2.373	2.185	2.325	2.417	1.914	1.821	2.573
La_2O_3	15.640	14.404	14.299	14.427	13.872	13.791	14.529	14.393	13.901	14.327	14.510	15.331
Ce_2O_3	28.506	28.227	28.249	27.904	26.964	26.803	27.229	27.089	27.253	28.047	28.391	27.771
Pr_2O_3	3.215	3.369	3.330	3.282	3.219	3.176	3.246	3.164	3.216	3.331	3.342	3.154
Nd_2O_3	11.593	12.486	12.484	12.589	11.895	11.826	11.722	11.587	12.059	12.166	12.407	11.634
Sm_2O_3	1.867	2.099	2.128	1.848	2.122	2.217	2.080	1.952	2.053	2.077	2.097	1.955
Eu_2O_3	0.172	0.062	0.025	0.029	0.122	0.077	0.059	0.097	0.060	0.062	0.138	0.182
Gd_2O_3	1.640	1.550	1.466	1.363	1.672	1.718	1.599	1.488	1.642	1.622	1.564	1.748
Tb_2O_3	0.133	0.110	0.130	0.078	0.166	0.136	0.150	0.141	0.139	0.193	0.081	0.190
Dy_2O_3	0.640	0.324	0.440	0.444	0.677	0.744	0.686	0.703	0.728	0.630	0.625	0.777
Ho_2O_3	0.059	0.000	0.060	0.016	0.065	0.096	0.081	0.063	0.085	0.077	0.071	0.027
Er_2O_3	0.349	0.287	0.326	0.371	0.432	0.395	0.457	0.447	0.428	0.443	0.406	0.407
Tm_2O_3	0.124	0.093	0.069	0.086	0.117	0.103	0.072	0.107	0.127	0.113	0.076	0.118
Yb_2O_3	0.115	0.107	0.124	0.116	0.188	0.166	0.176	0.168	0.144	0.165	0.175	0.160
Lu_2O_3	0.088	0.099	0.085	0.052	0.064	0.070	0.098	0.073	0.101	0.104	0.131	0.076
FeO	0.060	1.104	0.804	0.818	0.747	0.620	0.664	0.966	0.563	0.445	0.458	0.325
SO_3	0.016	0.018	0.014	0.018	0.015	0.019	0.029	0.010	0.024	0.016	0.007	0.027
CaO	0.681	1.036	0.826	0.778	1.085	1.059	1.009	1.041	0.974	0.850	0.741	0.828
SrO	0.009	0.020	0.023	0.021	0.027	0.035	0.000	0.022	0.010	0.003	0.004	0.026
SiO_2	0.216	0.286	0.322	0.644	0.162	0.165	0.156	0.152	0.173	0.146	0.160	0.203
Total	99.763	100.613	100.001	100.214	100.618	100.008	100.202	100.168	100.308	100.301	99.722	100.699
P	3.930	3.908	3.921	3.876	3.936	3.943	3.950	3.945	3.940	3.943	3.944	3.930
Si	0.034	0.046	0.051	0.103	0.025	0.026	0.025	0.024	0.027	0.023	0.025	0.032
Total T	3.964	3.953	3.972	3.979	3.961	3.969	3.974	3.969	3.967	3.966	3.969	3.962
Ca	0.115	0.177	0.141	0.133	0.183	0.179	0.170	0.177	0.164	0.144	0.126	0.139
Th	0.109	0.182	0.156	0.183	0.161	0.159	0.140	0.151	0.150	0.119	0.087	0.102
U	0.016	0.010	0.007	0.006	0.016	0.015	0.013	0.015	0.014	0.022	0.022	0.021
Pb	0.003	0.005	0.005	0.005	0.005	0.005	0.004	0.005	0.005	0.005	0.004	0.003
La	0.913	0.849	0.841	0.848	0.806	0.804	0.845	0.840	0.808	0.834	0.848	0.885
Ce	1.651	1.651	1.649	1.628	1.555	1.551	1.571	1.569	1.572	1.620	1.648	1.592
Pr	0.185	0.196	0.193	0.191	0.185	0.183	0.186	0.182	0.185	0.191	0.193	0.180
Nd	0.655	0.712	0.711	0.717	0.669	0.668	0.660	0.655	0.678	0.685	0.703	0.651
Sm	0.102	0.116	0.117	0.102	0.115	0.121	0.113	0.106	0.111	0.113	0.115	0.105
Eu	0.009	0.003	0.001	0.002	0.007	0.004	0.003	0.005	0.003	0.003	0.007	0.010
Gd	0.086	0.082	0.077	0.072	0.087	0.090	0.084	0.078	0.086	0.085	0.082	0.091
Tb	0.007	0.006	0.007	0.004	0.009	0.007	0.008	0.007	0.007	0.010	0.004	0.010
Dy	0.033	0.017	0.023	0.023	0.034	0.038	0.035	0.036	0.037	0.032	0.032	0.039
Ho	0.003	0.000	0.003	0.001	0.003	0.005	0.004	0.003	0.004	0.004	0.004	0.001
Er	0.017	0.014	0.016	0.019	0.021	0.020	0.023	0.022	0.021	0.022	0.020	0.020
Tm	0.006	0.005	0.003	0.004	0.006	0.005	0.004	0.005	0.006	0.006	0.004	0.006
Yb	0.006	0.005	0.006	0.006	0.009	0.008	0.008	0.008	0.007	0.008	0.008	0.008
Lu	0.004	0.005	0.004	0.003	0.003	0.003	0.005	0.003	0.005	0.005	0.006	0.004
Y	0.149	0.055	0.097	0.108	0.202	0.200	0.183	0.196	0.203	0.161	0.154	0.214
Total cat.	8.033	8.043	8.030	8.031	8.038	8.033	8.032	8.034	8.033	8.033	8.036	8.042
X_{LREE}	0.864	0.862	0.866	0.860	0.818	0.819	0.830	0.825	0.826	0.847	0.861	0.836
X_{HREE}	0.040	0.033	0.034	0.032	0.042	0.043	0.042	0.040	0.043	0.042	0.039	0.043
X_{hut}	0.003	0.005	0.007	0.015	0.000	0.000	0.000	0.000	0.001	0.000	0.000	0.000
X_{cher}	0.057	0.087	0.070	0.066	0.090	0.088	0.084	0.087	0.081	0.071	0.062	0.068
X_{xno}	0.037	0.013	0.024	0.027	0.050	0.049	0.045	0.048	0.050	0.040	0.038	0.052

Table S1 (continued)

Sample	VV-29	VV-29	VV-29	VV-29	VV-29	VV-29	VV-29	VV-29	VV-29	VV-29	VV-29	VV-29
Grain	mnz5/2	mnz5/3	mnz5/4	mnz5/5	mnz6/1	mnz6/2	mnz7/1	mnz7/2	mnz7a/1	mnz7a/2	mnz8/1	mnz8/2
							Fig. 10 A,B	Fig. 10 A,B				
Age, Ma	354.4	378.8	345.4	352.4	367.9	357.5	338.1	335.8	568.9	497.7	516.2	460.7
P_2O_5	29.594	29.147	29.113	29.289	29.507	29.696	30.307	29.603	31.145	30.606	29.714	29.908
PbO	0.090	0.076	0.072	0.074	0.082	0.100	0.086	0.087	0.069	0.114	0.118	0.098
ThO_2	3.563	2.982	3.067	3.092	3.523	3.851	4.140	4.293	2.392	4.786	4.217	3.878
UO_2	0.762	0.568	0.605	0.606	0.577	0.870	0.607	0.609	0.260	0.352	0.380	0.378
Y_2O_3	3.033	2.283	2.204	2.212	1.880	2.776	2.131	2.174	1.674	2.030	2.216	2.167
La_2O_3	14.539	15.462	15.602	15.466	15.136	14.409	14.461	14.622	14.513	13.136	14.429	14.603
Ce_2O_3	26.472	27.675	27.687	27.769	27.733	26.559	27.251	27.009	28.539	25.954	27.509	27.388
Pr_2O_3	2.917	3.195	3.078	3.133	3.230	3.031	3.344	3.222	3.377	3.037	3.226	3.165
Nd_2O_3	10.863	11.388	11.370	11.386	11.673	11.211	12.205	11.948	12.184	11.139	12.028	11.859
Sm_2O_3	2.016	2.000	1.859	1.943	1.983	1.976	2.146	2.155	2.173	2.047	2.095	2.080
Eu_2O_3	0.179	0.105	0.163	0.197	0.200	0.136	0.130	0.099	0.257	0.119	0.146	0.079
Gd_2O_3	2.014	1.696	1.684	1.655	1.754	1.704	1.902	1.971	1.409	1.615	1.747	1.656
Tb_2O_3	0.248	0.195	0.164	0.178	0.180	0.166	0.153	0.213	0.163	0.136	0.170	0.152
Dy_2O_3	1.155	0.767	0.707	0.756	0.750	0.815	0.778	0.775	0.548	0.745	0.703	0.692
Ho_2O_3	0.110	0.091	0.036	0.039	0.074	0.097	0.072	0.056	0.050	0.047	0.074	0.021
Er_2O_3	0.471	0.408	0.401	0.404	0.372	0.449	0.434	0.440	0.501	0.379	0.421	0.459
Tm_2O_3	0.124	0.116	0.105	0.102	0.098	0.082	0.115	0.086	0.102	0.043	0.095	0.134
Yb_2O_3	0.154	0.157	0.144	0.144	0.132	0.132	0.115	0.141	0.172	0.092	0.172	0.203
Lu_2O_3	0.089	0.057	0.118	0.101	0.117	0.084	0.108	0.062	0.143	0.134	0.081	0.079
FeO	0.256	0.215	0.255	0.239	0.341	0.318	0.623	0.543	1.807	2.462	1.402	1.335
SO_3	0.023	0.020	0.008	0.019	0.013	0.025	0.014	0.018	0.020	0.028	0.014	0.022
CaO	0.875	0.753	0.742	0.793	0.916	1.142	0.902	0.936	0.672	1.291	1.003	0.922
SrO	0.022	0.026	0.041	0.017	0.009	0.007	0.041	0.021	0.003	0.015	0.007	0.033
SiO_2	0.220	0.219	0.234	0.234	0.259	0.251	0.325	0.328	0.182	0.462	0.192	0.173
Total	99.786	99.599	99.456	99.847	100.538	99.886	102.390	101.410	102.352	100.769	102.157	101.484
P	3.943	3.918	3.920	3.923	3.923	3.944	3.950	3.917	4.041	4.029	3.932	3.960
Si	0.035	0.035	0.037	0.037	0.041	0.039	0.050	0.051	0.028	0.072	0.030	0.027
Total T	3.977	3.953	3.957	3.960	3.968	3.984	4.000	3.968	4.069	4.101	3.961	3.988
Ca	0.147	0.128	0.126	0.134	0.154	0.192	0.149	0.157	0.110	0.215	0.168	0.154
Th	0.128	0.108	0.111	0.111	0.126	0.137	0.145	0.153	0.083	0.169	0.150	0.138
U	0.027	0.020	0.021	0.021	0.020	0.030	0.021	0.021	0.009	0.012	0.013	0.013
Pb	0.004	0.003	0.003	0.003	0.003	0.004	0.004	0.004	0.003	0.005	0.005	0.004
La	0.844	0.905	0.915	0.902	0.878	0.834	0.821	0.843	0.820	0.753	0.832	0.842
Ce	1.525	1.609	1.612	1.608	1.596	1.525	1.536	1.545	1.601	1.478	1.574	1.568
Pr	0.167	0.185	0.178	0.181	0.185	0.173	0.188	0.183	0.189	0.172	0.184	0.180
Nd	0.611	0.646	0.646	0.643	0.655	0.628	0.671	0.667	0.667	0.619	0.671	0.662
Sm	0.109	0.109	0.102	0.106	0.107	0.107	0.114	0.116	0.115	0.110	0.113	0.112
Eu	0.010	0.006	0.009	0.011	0.011	0.007	0.007	0.005	0.013	0.006	0.008	0.004
Gd	0.105	0.089	0.089	0.087	0.091	0.089	0.097	0.102	0.072	0.083	0.091	0.086
Tb	0.013	0.010	0.009	0.009	0.009	0.009	0.008	0.011	0.008	0.007	0.009	0.008
Dy	0.059	0.039	0.036	0.039	0.038	0.041	0.039	0.039	0.027	0.037	0.035	0.035
Ho	0.006	0.005	0.002	0.002	0.004	0.005	0.004	0.003	0.002	0.002	0.004	0.001
Er	0.023	0.020	0.020	0.020	0.018	0.022	0.021	0.022	0.024	0.019	0.021	0.023
Tm	0.006	0.006	0.005	0.005	0.005	0.004	0.006	0.004	0.005	0.002	0.005	0.007
Yb	0.007	0.008	0.007	0.007	0.006	0.006	0.005	0.007	0.008	0.004	0.008	0.010
Lu	0.004	0.003	0.006	0.005	0.006	0.004	0.005	0.003	0.007	0.006	0.004	0.004
Y	0.254	0.193	0.187	0.186	0.157	0.232	0.175	0.181	0.137	0.168	0.184	0.180
Total cat.	8.026	8.044	8.040	8.041	8.039	8.034	8.012	8.034	7.970	7.969	8.039	8.020
X_{LREE}	0.807	0.846	0.848	0.846	0.842	0.805	0.831	0.827	0.870	0.805	0.829	0.836
X_{HREE}	0.055	0.044	0.042	0.043	0.044	0.044	0.046	0.047	0.039	0.041	0.043	0.043
X_{hut}	0.003	0.001	0.002	0.000	0.000	0.000	0.005	0.005	0.000	0.000	0.000	0.000
X_{cher}	0.073	0.063	0.062	0.066	0.076	0.094	0.074	0.077	0.056	0.110	0.082	0.077
X_{xno}	0.063	0.047	0.046	0.046	0.039	0.057	0.044	0.044	0.035	0.043	0.045	0.045

Table S1 (continued)

Sample	VV-29	VV-29	VV-29	VV-29	VV-29	VV-30	VV-30	VV-30	VV-30	VV-30	VV-30	VV-30
Grain	mnz9/1	mnz9/2	mnz9/3	mnz4/4	mnz4/5	mnz1/1	mnz2/1	mnz3/1	mnz3/2	mnz3/3	mnz3/4	mnz4/1
	Fig. 10F	Fig. 10F	Fig. 10F									
Age, Ma	330.1	344.9	345.6	488.0	507.1	505.7	497.3	352.7	354.7	360.2	353.3	388.2
P_2O_5	29.575	29.450	29.610	29.973	30.076	29.273	28.605	28.742	28.792	28.692	28.893	29.165
PbO	0.109	0.122	0.092	0.126	0.132	0.180	0.069	0.107	0.081	0.104	0.093	0.060
ThO_2	4.183	5.121	3.781	4.536	4.418	5.907	1.746	5.222	4.052	5.173	4.031	1.049
UO_2	1.168	1.040	0.818	0.490	0.542	0.789	0.509	0.631	0.465	0.545	0.696	0.846
Y_2O_3	2.362	2.114	1.800	2.682	2.699	1.919	1.460	2.330	1.846	2.009	2.526	2.260
La_2O_3	15.138	14.959	15.211	13.973	14.040	12.740	15.159	16.388	16.381	16.940	15.282	18.469
Ce_2O_3	26.789	26.763	27.932	26.676	26.855	26.004	29.460	26.434	28.170	26.767	27.282	29.157
Pr_2O_3	3.003	3.042	3.142	3.291	3.206	3.150	3.464	2.907	3.091	2.883	3.074	3.012
Nd_2O_3	11.315	10.946	11.491	12.009	11.891	11.572	12.429	10.349	10.977	10.339	11.229	10.513
Sm_2O_3	1.926	1.800	1.941	2.133	2.090	2.233	1.904	1.666	1.685	1.530	1.917	1.704
Eu_2O_3	0.134	0.149	0.133	0.062	0.125	0.188	0.302	0.140	0.139	0.102	0.122	0.147
Gd_2O_3	1.833	1.708	1.745	1.625	1.694	1.950	1.280	1.607	1.424	1.433	1.568	1.744
Tb_2O_3	0.168	0.206	0.174	0.175	0.125	0.184	0.089	0.221	0.111	0.194	0.142	0.129
Dy_2O_3	0.802	0.810	0.703	0.783	0.803	0.704	0.529	0.694	0.615	0.662	0.711	0.758
Ho_2O_3	0.025	0.005	0.049	0.085	0.037	0.029	0.035	0.025	0.061	0.021	0.051	0.068
Er_2O_3	0.404	0.423	0.385	0.433	0.445	0.391	0.395	0.415	0.381	0.423	0.460	0.417
Tm_2O_3	0.137	0.117	0.136	0.146	0.119	0.093	0.099	0.116	0.118	0.100	0.125	0.043
Yb_2O_3	0.123	0.098	0.078	0.170	0.187	0.141	0.119	0.108	0.080	0.147	0.134	0.095
Lu_2O_3	0.035	0.063	0.085	0.074	0.085	0.052	0.082	0.077	0.087	0.104	0.097	0.071
FeO	0.348	0.272	0.288	0.646	0.547	1.069	1.161	0.279	0.243	0.395	0.491	0.018
SO_3	0.038	0.019	0.034	0.011	0.017	0.020	0.021	0.021	0.028	0.031	0.032	0.012
CaO	1.243	1.277	0.999	1.070	1.049	1.448	0.543	1.125	0.862	1.079	1.093	0.433
SrO	0.025	0.024	0.032	0.003	0.004	0.037	0.026	0.005	0.029	0.040	0.021	0.016
SiO_2	0.271	0.350	0.272	0.218	0.199	0.329	0.199	0.424	0.368	0.431	0.304	0.190
Total	101.154	100.877	100.928	101.388	101.385	100.404	99.685	100.032	100.086	100.143	100.371	100.374
P	3.913	3.907	3.926	3.945	3.951	3.925	3.904	3.867	3.877	3.867	3.879	3.899
Si	0.042	0.055	0.043	0.034	0.031	0.052	0.032	0.067	0.059	0.069	0.048	0.030
Total T	3.955	3.962	3.968	3.979	3.982	3.977	3.936	3.935	3.936	3.936	3.927	3.929
Ca	0.208	0.214	0.168	0.178	0.174	0.246	0.094	0.192	0.147	0.184	0.186	0.073
Th	0.149	0.183	0.135	0.160	0.156	0.213	0.064	0.189	0.147	0.187	0.145	0.038
U	0.041	0.036	0.028	0.017	0.019	0.028	0.018	0.022	0.016	0.019	0.025	0.030
Pb	0.005	0.005	0.004	0.005	0.006	0.008	0.003	0.005	0.003	0.004	0.004	0.003
La	0.873	0.865	0.879	0.801	0.804	0.744	0.901	0.961	0.961	0.995	0.894	1.076
Ce	1.533	1.536	1.602	1.518	1.526	1.508	1.739	1.538	1.640	1.560	1.584	1.686
Pr	0.171	0.174	0.179	0.186	0.181	0.182	0.203	0.168	0.179	0.167	0.178	0.173
Nd	0.632	0.613	0.643	0.667	0.659	0.655	0.715	0.587	0.624	0.588	0.636	0.593
Sm	0.104	0.097	0.105	0.114	0.112	0.122	0.106	0.091	0.092	0.084	0.105	0.093
Eu	0.007	0.008	0.007	0.003	0.007	0.010	0.017	0.008	0.008	0.006	0.007	0.008
Gd	0.095	0.089	0.091	0.084	0.087	0.102	0.068	0.085	0.075	0.076	0.082	0.091
Tb	0.009	0.011	0.009	0.009	0.006	0.010	0.005	0.012	0.006	0.010	0.007	0.007
Dy	0.040	0.041	0.035	0.039	0.040	0.036	0.027	0.036	0.032	0.034	0.036	0.039
Ho	0.001	0.000	0.002	0.004	0.002	0.001	0.002	0.001	0.003	0.001	0.003	0.003
Er	0.020	0.021	0.019	0.021	0.022	0.019	0.020	0.021	0.019	0.021	0.023	0.021
Tm	0.007	0.006	0.007	0.007	0.006	0.005	0.005	0.006	0.006	0.005	0.006	0.002
Yb	0.006	0.005	0.004	0.008	0.009	0.007	0.006	0.005	0.004	0.007	0.006	0.005
Lu	0.002	0.003	0.004	0.003	0.004	0.002	0.004	0.004	0.004	0.005	0.005	0.003
Y	0.196	0.176	0.150	0.222	0.223	0.162	0.125	0.197	0.156	0.170	0.213	0.190
Total cat.	8.052	8.044	8.038	8.027	8.024	8.037	8.058	8.061	8.058	8.060	8.071	8.060
X_{LREE}	0.807	0.807	0.839	0.813	0.814	0.793	0.891	0.813	0.850	0.824	0.819	0.877
X_{HREE}	0.044	0.043	0.042	0.043	0.043	0.045	0.033	0.041	0.036	0.039	0.041	0.041
X_{hut}	0.000	0.002	0.000	0.001	0.001	0.001	0.000	0.006	0.005	0.007	0.000	0.000
X_{cher}	0.101	0.105	0.082	0.088	0.086	0.121	0.045	0.093	0.071	0.089	0.089	0.035
X_{xno}	0.048	0.043	0.037	0.055	0.055	0.040	0.030	0.048	0.038	0.041	0.051	0.046

Table S1 (continued)

| Sample | VV-30 | VV-30 | VV-30 | VV-30 | VV-30 | VV-30 | VV-30 | VV-30 |
Grain	mnz4/2	mnz4/3	mnz4/4	mnz4/5	mnz4/6	mnz4/7	mnz4/8	mnz5/1
Age, Ma	369.3	381.9	350.6	362.9	395.5	400.0	374.7	347.6
P_2O_5	29.056	29.147	29.108	29.101	29.108	29.219	29.208	28.901
PbO	0.058	0.068	0.071	0.066	0.066	0.066	0.060	0.104
ThO_2	1.081	1.198	1.125	1.193	1.212	1.155	1.129	3.352
UO_2	0.846	0.969	1.169	0.992	0.868	0.872	0.862	1.178
Y_2O_3	2.304	2.403	2.547	2.369	2.297	2.148	2.238	2.463
La_2O_3	18.404	18.222	18.113	18.425	18.277	18.723	18.533	16.072
Ce_2O_3	28.656	28.618	28.426	28.552	28.601	28.924	28.775	27.222
Pr_2O_3	2.931	2.988	2.926	2.892	3.053	2.988	3.016	2.961
Nd_2O_3	10.371	10.232	10.377	10.273	10.415	10.357	10.335	10.650
Sm_2O_3	1.722	1.728	1.727	1.766	1.750	1.620	1.643	2.040
Eu_2O_3	0.163	0.138	0.180	0.121	0.131	0.141	0.168	0.126
Gd_2O_3	1.706	1.769	1.733	1.778	1.713	1.655	1.669	2.129
Tb_2O_3	0.155	0.127	0.181	0.170	0.244	0.161	0.170	0.207
Dy_2O_3	0.750	0.819	0.789	0.813	0.783	0.730	0.726	0.916
Ho_2O_3	0.034	0.107	0.074	0.032	0.038	0.037	0.047	0.077
Er_2O_3	0.442	0.431	0.406	0.381	0.435	0.389	0.425	0.418
Tm_2O_3	0.065	0.091	0.097	0.068	0.062	0.130	0.090	0.122
Yb_2O_3	0.111	0.113	0.156	0.120	0.173	0.122	0.167	0.129
Lu_2O_3	0.085	0.067	0.096	0.067	0.039	0.085	0.125	0.100
FeO	0.023	0.019	0.028	0.003	0.000	0.052	0.045	0.097
SO_3	0.022	0.030	0.017	0.020	0.012	0.022	0.026	0.020
CaO	0.426	0.635	0.709	0.475	0.448	0.481	0.442	0.835
SrO	0.006	0.015	0.009	0.043	0.005	0.000	0.004	0.011
SiO_2	0.199	0.207	0.206	0.264	0.185	0.179	0.204	0.375
Total	99.615	100.139	100.271	99.985	99.914	100.253	100.105	100.501
P	3.906	3.898	3.890	3.898	3.904	3.907	3.908	3.871
Si	0.032	0.033	0.033	0.042	0.029	0.028	0.032	0.059
Total T	3.938	3.931	3.923	3.940	3.934	3.935	3.940	3.930
Ca	0.072	0.107	0.120	0.081	0.076	0.081	0.075	0.142
Th	0.039	0.043	0.040	0.043	0.044	0.041	0.041	0.121
U	0.030	0.034	0.041	0.035	0.031	0.031	0.030	0.041
Pb	0.002	0.003	0.003	0.003	0.003	0.003	0.003	0.004
La	1.078	1.062	1.055	1.075	1.068	1.091	1.080	0.938
Ce	1.666	1.655	1.643	1.654	1.659	1.672	1.665	1.577
Pr	0.170	0.172	0.168	0.167	0.176	0.172	0.174	0.171
Nd	0.588	0.577	0.585	0.580	0.589	0.584	0.583	0.602
Sm	0.094	0.094	0.094	0.096	0.096	0.088	0.089	0.111
Eu	0.009	0.007	0.010	0.007	0.007	0.008	0.009	0.007
Gd	0.090	0.093	0.091	0.093	0.090	0.087	0.087	0.112
Tb	0.008	0.007	0.009	0.009	0.013	0.008	0.009	0.011
Dy	0.038	0.042	0.040	0.041	0.040	0.037	0.037	0.047
Ho	0.002	0.005	0.004	0.002	0.002	0.002	0.002	0.004
Er	0.022	0.021	0.020	0.019	0.022	0.019	0.021	0.021
Tm	0.003	0.004	0.005	0.003	0.003	0.006	0.004	0.006
Yb	0.005	0.005	0.008	0.006	0.008	0.006	0.008	0.006
Lu	0.004	0.003	0.005	0.003	0.002	0.004	0.006	0.005
Y	0.195	0.202	0.214	0.199	0.194	0.181	0.188	0.207
Total cat.	8.054	8.068	8.076	8.056	8.055	8.057	8.053	8.061
X_{LREE}	0.876	0.857	0.848	0.869	0.872	0.876	0.875	0.824
X_{HREE}	0.042	0.043	0.043	0.043	0.044	0.041	0.043	0.051
X_{hut}	0.000	0.000	0.000	0.000	0.000	0.000	0.000	0.006
X_{cher}	0.035	0.052	0.057	0.039	0.037	0.039	0.036	0.069
X_{xno}	0.047	0.049	0.051	0.048	0.047	0.044	0.046	0.050